

## Early Holocene relative sea-level changes on the central east coast of the Yellow Sea

Dong-Yoon Yang<sup>a</sup>, Min Han<sup>a,\*</sup>, Hyun Ho Yoon<sup>a</sup>, Ara Cho<sup>a</sup>, Jin Cheul Kim<sup>a</sup>, Eunseo Choi<sup>b,\*</sup>, Kaoru Kashima<sup>c</sup>

<sup>a</sup> Quaternary Environment Research Center, Korea Institute of Geoscience and Mineral Resources, 124 Gwahak-ro, Yuseong-gu, Daejeon 34132, Republic of Korea

<sup>b</sup> Center for Earthquake Research and Information, the University of Memphis, 3890 Central Ave, Memphis, TN 38152, USA

<sup>c</sup> Department of Earth & Planetary Science, Kyushu University, 744 Motooka, Fukuoka 819-0395, Japan

### ARTICLE INFO

Editor: M Elliot

#### Keywords:

Early Holocene  
Relative Sea level change  
Basal peat  
GIA model  
Diatom

### ABSTRACT

Paleo-relative sea level (paleo-RSL) records in the far-field are essential for constraining models for global sea level change. We compared the early Holocene RSL history on the central east coast of the Yellow Sea with those of Bohai Bay, the northernmost point, and Gunsan Bay, south of the study area. A multi-proxy approach, including lithostratigraphy, biostratigraphy, combined with radiocarbon and OSL dating, facilitated the generation of 28 sea level index points (SLIPs) using 11 borehole samples. Excavation of basal peat of the 10.3 ka in the study area established that the observed RSL of the transgression in the early Holocene was  $-14.88$  m, which was much shallower than  $-27.9$  m in Gunsan Bay at 9.8 ka and was similar to  $-17.3$  m in Bohai Bay at 9.7 ka. The observed RSL and the prediction curves of the study area were compared with those of other areas. In Gunsan Bay, the early Holocene GIA prediction curves are consistent with those observed, which seems to be the result of a “low setting” of the crust thickness and mantle viscosity. Therefore, it is presumed that the significant difference in the elevations observed between the study area and Gunsan Bay is caused by the levering effect owing to the difference in the tectonic characteristics. Conversely, other observed groups during 7.6–6 ka have a similar slope to the prediction curve of the Early Holocene in the study site, and it is thought that the sediments of the early Holocene were eroded and re-deposited along the channel. These results are of great importance as data of sea level variability in the far field due to glacial collapse and as data for the GIA modeling process.

### 1. Introduction

The threat of sea level rise to the heavily populated Korean Peninsula, which contains approximately 15,000 km of coastline bordering open sea margins, has a profound and far-reaching implications. Trends in sea level rise by using satellite altimetry on the Korean Peninsula are well above the global average trend (Watson and Lim, 2020). The changing rate of mean sea level occurred by natural factors such as global warming varies from 1.1 mm/y in the north to 4.4 mm/y in the south in the western coast of the Korean peninsula (Jung, 2014). Data on rapid sea level rise during the early Holocene will play an important role in predicting future sea level fluctuations. Given the importance of agricultural and industrial production on the east coast of China and on the Korean Peninsula, studies on the Yellow Sea coast is urgently needed to understand past sea level changes in the region (e.g., Yokoyama and

Purcell, 2021).

Rapid sea level rise in the early Holocene ( $-8.2$  ka; Walker et al., 2012) and gradual rise in the mid-Holocene (8.2–4.2 ka; Walker et al., 2012) have been frequently reported in previous studies (Bloom and Park, 1985; Korea Ocean Research and Development Institute, 1994; Kim et al., 1999; Chang et al., 1996; Chang and Choi, 2001; Lee and Chang, 2015). Most of the cores used in such studies were collected from the subtidal zone or lower. While other studies using terrestrial cores have suggested that local sea level has been higher than the present levels during the mid-Holocene (Nahm and Hong, 2014; Bak, 2015; Park et al., 2015). However, these papers are missing information from viewpoints of hydro-isostatic adjustment (Song et al., 2018). Moreover, most papers did not provide evidence such as basal peat to indicate the onset of the early Holocene transgression. In particular, in coastal areas, it is difficult to preserve intact sedimentary layers owing to erosion, and

\* Corresponding authors.

E-mail addresses: [ydy@kigam.re.kr](mailto:ydy@kigam.re.kr) (D.-Y. Yang), [hanmin@kigam.re.kr](mailto:hanmin@kigam.re.kr) (M. Han), [hhyoon@kigam.re.kr](mailto:hhyoon@kigam.re.kr) (H.H. Yoon), [joara5813@kigam.re.kr](mailto:joara5813@kigam.re.kr) (A. Cho), [kjc76@kigam.re.kr](mailto:kjc76@kigam.re.kr) (J.C. Kim), [echoi2@memphis.edu](mailto:echoi2@memphis.edu) (E. Choi), [kashima@geo.kyushu-u.ac.jp](mailto:kashima@geo.kyushu-u.ac.jp) (K. Kashima).

<https://doi.org/10.1016/j.palaeo.2022.111185>

Received 11 April 2022; Received in revised form 23 June 2022; Accepted 6 August 2022

Available online 10 August 2022

0031-0182/© 2022 The Authors. Published by Elsevier B.V. This is an open access article under the CC BY license (<http://creativecommons.org/licenses/by/4.0/>).

basal peat is rarely preserved even in semi-enclosed shores. However, recently, paleo-sea level change studies of Bohai Bay on the northwest coast and Gunsan Bay on the east coast of the Yellow Sea were published (Wang et al., 2020; Song et al., 2018). The study site is located on the mid-east coast of Yellow Sea, and Bohai Bay and Gunsan Bay are 800 km to the northwest and 140 km to the south from the study site, respectively. Although the study site and Gunsan Bay are close, there is a big elevation difference in the observed relative sea level (RSL) of the transgression between the two sites in the early Holocene. Changes in RSL are caused by a combination of global (glacio-eustatic) sea-level changes and regional land movement (Meijles et al., 2018). Geological observations of postglacial relative land- and sea-level change in NW Europe constrain models of glacial isostatic adjustment (GIA) (e.g., Lambeck et al., 1998), which in turn are used to understand Earth structure and viscosity parameters of lithosphere and mantle (Vink et al., 2008).

We obtained the relative observed Holocene Sea level data at the study site and compared it with the predicted sea-level of the GIA model to confirm the suitability of the data. In addition, the causes of similarities and differences were analyzed by comparing this data with those from Bohai Bay and Gunsan Bay, respectively. The results of this study will be important data for the study of the RSL changes in the Yellow Sea, as the far-field of the Western Pacific. GIA models also provide data on vertical coastal land movements for input into future RSL change scenarios (Lowe et al., 2018; Simpson et al., 2017).

## 2. Site description

The Korean Peninsula can be divided into seven major tectonic provinces, i.e., from northwest to southeast, the Nangrim massif, Pyeongnam Basin, Imjingang belt, Gyeonggi massif, Ogcheon belt, Yeongnam massif, and Gyeongsang Basin (Koh et al., 2015; Liu and Zhou, 2019). Chang (2013) suggested that the Sulu subduction-collision zone does not extend toward the Korean Peninsula because of the Paleozoic Yellow Sea Transform Fault. However, Nd model age data currently support that the Gyeonggi massif might have a close affinity to the Jiaobei terrane in the North China Craton, and the Ogcheon belt agrees well with the Sulu terrane. In contrast, the Yeongnam massif is more closely linked to the South China Craton (Liu and Zhou, 2019). The study area corresponds to the Gyeonggi Massif, and Gunsan area belongs to the Okcheon belt. Conversely, the Bohai region is included in the Eastern Block of the craton of North China (Fig. 1a).

The International Hydrographic Organization (1953) defines the limits of the Yellow Sea (which it also names as “Hwang Hai”) as follows: The Yellow Sea is separated from the South Sea by the boundary from the southern end of Haenam Peninsula in Jeollanamdo to Jeju Island and divided into the East China Sea by the boundary from the west end of Jeju Island to the Yangtze River estuary. The Yellow Sea is a semi-enclosed, continental shelf embayment surrounded by mainland China and Korean Peninsula. It joins the Bohai Sea in the north and the East China Sea in the south. The Yellow Sea has an average water depth of approximately 55 m and a maximum depth of approximately 100 m at its south-eastern margin, and flat and broad seafloor (Chough et al., 2000). The western part of the Yellow Sea includes deltas of the Huanghe River and the isobaths are parallel to the coastline, whereas in the eastern part Yellow Sea, the Korean Peninsula is characterized by rias and over 3000 islands along its western and southern coasts (Chough, 2013). The seafloor deepens progressively to the southeast along the NW–SE axis of the former late Pleistocene low stand shorelines (Fig. 1b, Chough et al., 2004). Eustatic sea-level fluctuations during the Quaternary had a great effect on sedimentation in the Yellow Sea (Chough et al., 2000; Jin et al., 2002; Shinn et al., 2007; Yoo et al., 2016). Off the Jiangsu coast, the shallow and flat seafloor forms in water depth of 50 m and slopes gently eastward to the central part of the sea (Fig. 1b, Chough et al., 2004).

The Yellow Sea receives huge volume of water discharge and

sediment load from the Huanghe (1080 Mt. yr<sup>-1</sup>) and Changjing (480 Mt. yr<sup>-1</sup>) Rivers (Milliman and Syvitski, 1992). There are many small rivers from China and Korea Peninsula debouched into the Yellow Sea. The Korean rivers (e.g. Han, Geum and Yeongsan Rivers) annually delivered a total of 5–25 Mt. sediment to the Yellow Sea (Lim et al., 2007). Tides are typically semi-diurnal (M2) in the Yellow Sea ranging from 1.5 m to 8 m (Chough et al., 2000), and rates of tidal currents vary from lower than 40 cm/s in the central parts of the north and south Yellow Sea to over 100 cm/s in the southwest and northeast Yellow Sea (Liu et al., 2007). Tide range is generally higher than 3 m and up to 8 m along west Korean coast, and about 2–4 m along Chinese coast (Liu et al., 2007). Tidal currents in the eastern Yellow Sea flow northward during flood, while mostly south or southwestward during ebb (Park and Lee, 1994; Lee and Chu, 2001).

Tide-dominated estuaries are common along the macro-tidal coasts of Europe, the United Kingdom, Canada, China and northern Australia. In this chapter we refer to the Scheldt, Severn, Ord and Logan River estuaries as examples of tide-dominated systems. Tide-dominated estuaries are characterized by a funnel-shaped mouth, giving way to channelized upper estuary and tidal river reaches (Boyd et al., 1991; Dalrymple et al., 1992; Scanes et al., 2017). The western coast of Korean Peninsula is characterized by a typical ria-type coast in macrotidal embayment. The Asan Estuary, located at the southern part of Gyeonggi Bay, is a tide-dominated estuary having a main tidal channel with a maximum depth of 30 m below the mean low-water level and central sand ridge (Chang et al., 2011). Along with the main tidal channel system in the Asan Estuary, small-scale tidal-fluvial channels such as Namyang Bay and Tando Estuary flow into the Asan Estuary, and the intertidal flat is widely developed around the branch channels. The surface sedimentary facies and tidal flat sequence of the Namyang Bay, which is adjacent to the study area, were known through the several studies (Alexander et al., 1991; Lim et al., 2003). Namyang Bay is a funnel-shaped embayment in the east-west direction with a length of 12 km and a width of 3 to 9 km. The tidal range is 8.3 m at high tide and 4.9 m at low tide (mean tidal range of 5.7 m) (Lim et al., 2003). The main channel has a maximum depth of 25 m and a width of approximately 1 to 2 km from bay-mouth area, and the axis is approximately east-west-oriented. The surface sediments of intertidal flats show a gradually finer distribution from the main tidal channel toward the upland (Alexander et al., 1991; Lim et al., 2003). Small amount of sediment are supplied through two tidal-fluvial channels that flow into the Namyang Bay. The stratigraphic evolutions of the intertidal facies in the Namyang Bay shows a typical tidal flat succession of the mid- to late Holocene showing coarsening upward and retrograding sequence (Lim et al., 2003).

The study site, the Tando Estuary mouth is located near Jeongok Port, Hwaseong City, 50 km southwest of Seoul. Most of the study site is currently used as reclaimed land, but the topographical features show the characteristics of the mouth of the estuary systems, which corresponds to the outer estuary. In this area, tidal flats are well developed under the influence of a macro-tidal regime (Han et al., 2017). The subtidal channels in the Tando Estuary mouth are generally flanked by an extensive and diverse array of intertidal and supratidal habitats (salt flat and salt marsh like Fig. 3 of Scanes et al., 2017). Currently, after embankments have been built in the southern (Tando) and northern (Sihwa) regions of the Hwaseong coast, the tidal channels and flats from which seawater has flowed are used as irrigation channels (Fig. 1d). In addition, most of the intertidal and supratidal area located inside embankments are already reclaimed (Fig. 1d).

## 3. Methods

In this study, a total of eleven cores were obtained from the Tando Estuary off the coast of Hwaseong (Figs. 1d and 2). First, the DS17–09 core site is presumed to be a freshwater swamp before embankment construction (Fig. 1d). Drilling was conducted from an altitude of 7.07 m

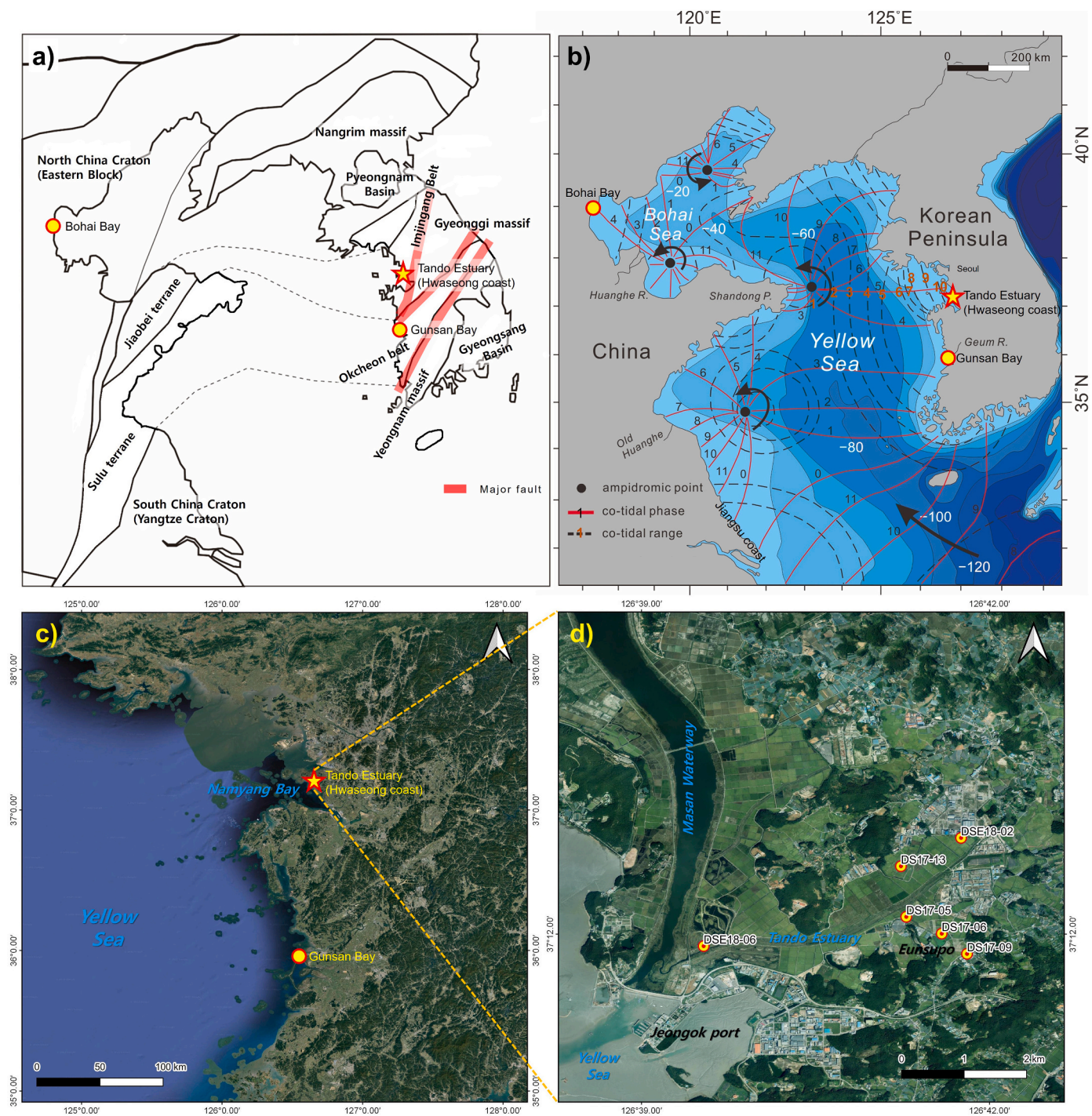


**Fig. 1.** Study area map. The yellow circles are the reference sites and the yellow star is the study site named the Tando Estuary in the Hwaseong City coastal area. a) The sketch geological map showing the tectonic relationships between South Korea and China modified from Fig. 10 of Liu and Zhou (2019). The Gyeonggi massif might have a close affinity to the Jiaobei terrane in the North China Craton, and the Okcheon belt agrees well with the Sulu terrane. The study area corresponds to the Gyeonggi massif, and Gunsan area belongs to the Okcheon belt. Conversely, the Bohai region is included in the Eastern Block of the North China Craton. b) Current tidal range information map of the Yellow Sea. Observed tides in the Yellow Sea (M2 tidal only) modified Cummings et al. (2015). The tidal current moves northward into the Yellow Sea from the Pacific Ocean. As it shoals across the shelf edge, it shortens in wavelength and is amplified, and then banks up against the right-hand (eastern) side of the Yellow Sea basin due to the Coriolis effect. This generates meso- to macro-tidal conditions along the west Korean coast. The reflected tidal wave moves out of the Yellow Sea along the Chinese coast. Interference of incoming and reflected waves produces four amphidromic systems in the Yellow and Bohai Seas. Because of tidal friction and energy dissipation, the reflected wave is weaker than the incoming wave, displacing the amphidromic points toward the Chinese coast. c) Satellite image map in the middle part of west coast of the Korean Peninsula included in the Hwaseong coast and Gunsan Bay. d) Satellite image map in the Tando Estuary include core locations. (For interpretation of the references to colour in this figure legend, the reader is referred to the web version of this article.)

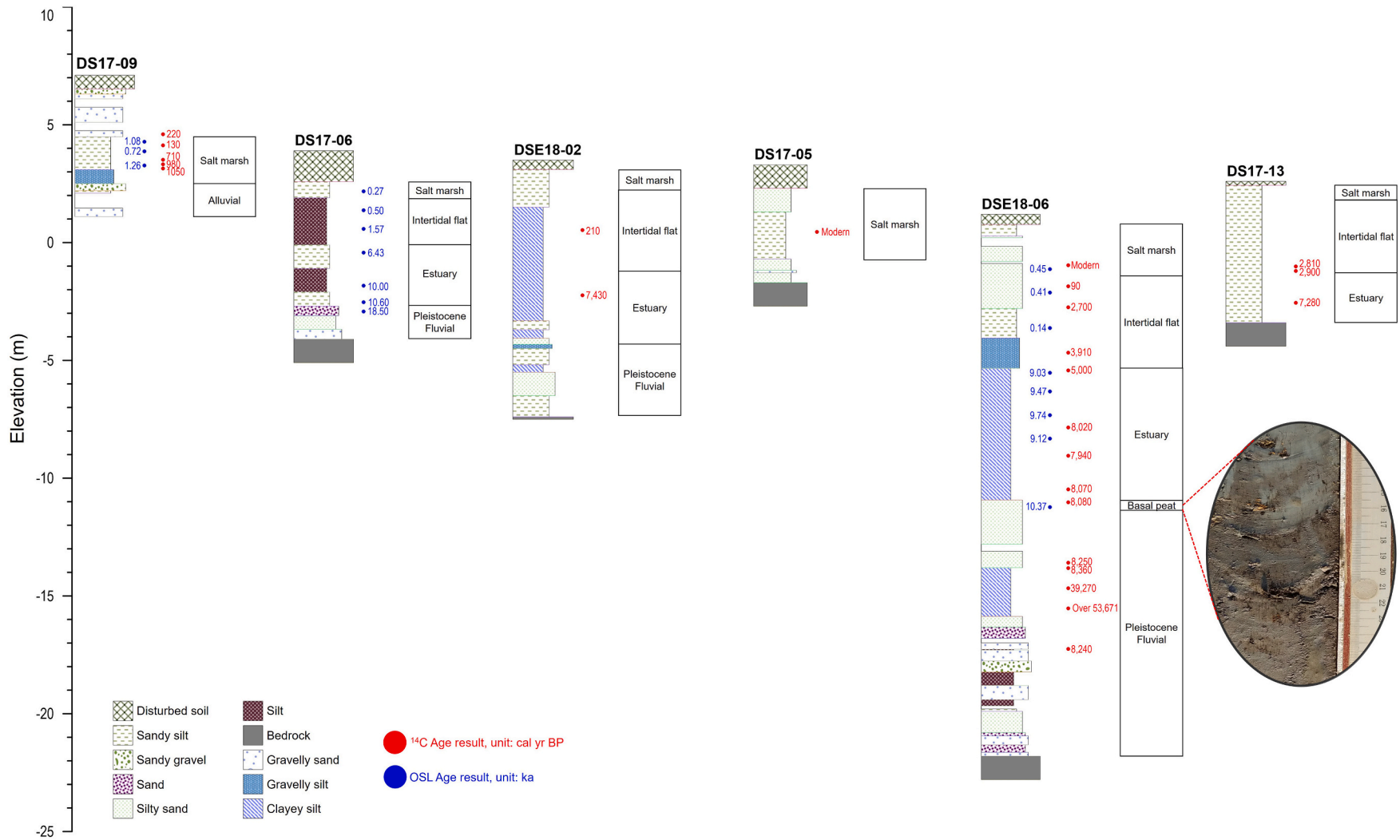


**Fig. 2.** Cross section of a core series on the Tando Estuary in the Hwaseong coast. Sedimentary facies and age dating results are shown together.

to a depth of 6 m (Fig. 2). Second, the site of DS17–06 is estimated as a salt marsh environment around intertidal flat (Fig. 1d). In this core, drilling was performed at an elevation of 3.9 m to a depth of 9 m (Fig. 2). Third, the DSE18–02, DS17–05 and DSE18–06 cores are obtained around the tidal channel (Fig. 1d). The DSE18–02 site, the highest point of the tidal channel, was excavated from an elevation of 3.5 m to a depth of 11 m (Fig. 2). The DS17–05 core was drilled to a depth of 6 m from an elevation of 3.3 m at the point where it joined the main channel (Figs. 1d and 2). The DSE18–06 core site corresponds to the downstream of the tidal channel and is located at the junction with the Masan waterway (Fig. 1d). This core was drilled from an altitude of 1.2 m to a depth of 24 m (Fig. 2). Finally, the DS17–13 site is opposite the estuary (Fig. 1d). Drilling was conducted from an altitude of 2.6 m to a depth of 7 m (Fig. 2). In addition, five boreholes of DSE18–03, DSE18–4 and DS17–14 located between DSE18–02 and DSE18–06, and DS17–07 and DSA17–4 located near DS17–06 have been added for comparison with already selected boreholes' sediments. The first three core sediments have typical channel sediment characteristics and in DS17–07, channel sediments were also confirmed in the –3.5–4.5 m in elevation section. That is, it is a sedimentary unit of alternating with silt and fine sand, often containing wood and rock fragments or gravels. The last borehole contains organic matter typical of salt marshes.

### 3.1. Age dating: Radiocarbon and optically stimulated luminescence

Radiocarbon ( $^{14}\text{C}$ ) and OSL (optically stimulated luminescence) age dating were performed to confirm the ages of sedimentary environment changes in the Tando Estuary of the Hwaseong coast. First, a total of 25 radiocarbon age dating samples were collected from 5 cores, excluding

the DS17–06 (Table 1). The object of radiocarbon dating was terrestrial plant fragments included horizontally in the deposit layer. However, some of the plant roots were also included in the analysis for comparison with other dating results, which were contained at a vertical or inclined angle with the sediment layer. The collected samples were subjected to a series of chemical pretreatments and oxidation-reduction processes to produce graphite targets. The  $^{14}\text{C}$  ages were measured using the AMS (accelerator mass spectrometry) possessed by Korea Institute of Geoscience and Mineral Resources (KIGAM) for the finished graphite targets. The  $^{14}\text{C}$  ages were calculated and converted to calendar dates by using IntCal13 (Reimer et al., 2013) and OxCal v4.3.2 (Ramsey, 2017) (Table 1).

OSL samples were collected on each borehole after removing uppermost light exposed surface sediments (Table 2). OSL measurement was applied to chemically purified quartz grains (4–11  $\mu\text{m}$  in diameter). The fine-grained samples were chemically treated with sodium pyrophosphate to disperse and remove clays. They were also treated with 10% hydrochloric acid and 30% hydrogen peroxide to remove carbonate and organic materials, respectively. Chemically treated samples were settled in dilute sodium oxalate solution for obtaining the 4–11  $\mu\text{m}$  grain-size fraction. To remove any feldspar grains, hydrofluorosilicic acid etching for 2 weeks were used (Kim et al., 2021).

In borehole DSE18–06, luminescence signals were measured using a Risø luminescence reader (TL/OSL-DA-20; Risø DTU, Roskilde, Denmark) equipped with a blue light-emitting diode (LED) ( $470 \pm 20$  nm) stimulation source and  $0.104 \text{ Gy s}^{-1} \text{ }^{90}\text{Sr}/^{90}\text{Y}$  beta irradiation source. In boreholes DS 17–06 and DS 17–09, luminescence signals were measured using a Lexsyg smart system TL/OSL reader (Freiberg Instruments, Freiberg, Germany) equipped with a blue LED ( $458 \pm 5$  nm)

**Table 1**

$^{14}\text{C}$  age dating results in the coastal area of Hwaseong City.

Borehole Name	Sample Lab. No.	Material	Depth/ Elevation (m)	$^{14}\text{C}$ Age (BP)	$\delta^{13}\text{C}$	$\Delta^{14}\text{C}$ (‰)	Curve data	Calendar age (yr)
DS17–05	KGM-IWd180260	Plant	2.85/0.45	Modern	$-27.57 \pm 0.20$	$327.74 \pm 4.59$	Oxcal v4.3.2	After 1950 CE
DS17–07	KGM-IWd180261	Plant	8.68/–4.38	$7430 \pm 50$	$-29.03 \pm 0.75$	$-606.59 \pm 2.32$	Oxcal v4.3.2	$5480 \text{ BCE} \pm 50$
DS17–07	KGM-IWd180262	Plant	8.93/–4.63	$7490 \pm 50$	$-28.56 \pm 0.47$	$-609.82 \pm 2.31$	Oxcal v4.3.2	$5540 \text{ BCE} \pm 50$
DS17–09	KGM-IWd180264	Plant	2.50/4.60	$220 \pm 30$	$-26.78 \pm 0.11$	$-34.44 \pm 3.78$	Oxcal v4.3.2	$1730 \text{ CE} \pm 30$
DS17–09	KGM-IWd180265	Plant	2.97/4.13	$130 \pm 30$	$-24.66 \pm 0.43$	$-23.76 \pm 3.81$	Oxcal v4.3.2	$1820 \text{ CE} \pm 30$
DS17–09	KGM-IWd180266	Plant	3.59/3.51	$710 \pm 50$	$-33.63 \pm 0.36$	$-92.52 \pm 5.59$	Oxcal v4.3.2	$1240 \text{ CE} \pm 50$
DS17–09	KGM-IWd180268	Plant	3.78/3.32	$980 \pm 40$	$-31.95 \pm 0.28$	$-121.60 \pm 4.36$	Oxcal v4.3.2	$970 \text{ CE} \pm 40$
DS17–09	KGM-IWd180269	Plant	3.95/3.15	$1050 \pm 40$	$-29.72 \pm 0.14$	$-130.25 \pm 4.47$	Oxcal v4.3.2	$900 \text{ CE} \pm 40$
DS17–13	KGM-IWd180273	Plant	3.61/–1.01	$2810 \pm 40$	$-25.70 \pm 0.28$	$-301.34 \pm 3.16$	Oxcal v4.3.2	$860 \text{ BCE} \pm 40$
DS17–13	KGM-IWd180274	Plant	3.80/–1.20	$2900 \pm 40$	$-28.07 \pm 0.28$	$-308.80 \pm 3.21$	Oxcal v4.3.2	$950 \text{ BCE} \pm 40$
DS17–13	KGM-IWd180318	Plant	5.16/–2.56	$7280 \pm 50$	$-31.20 \pm 1.51$	$-599.20 \pm 2.28$	Oxcal v4.3.2	$5330 \text{ BCE} \pm 50$
DS17–14	KGM-IWd180275	Plant	6.55/–3.85	$6450 \pm 50$	$-29.64 \pm 0.19$	$-555.66 \pm 2.48$	Oxcal v4.3.2	$4500 \text{ BCE} \pm 50$
DSA17–04	KGM-IWd180339	Plant	2.04/1.66	$8060 \pm 40$	$-29.87 \pm 2.30$	$-6.36.42 \pm 2.01$	Oxcal v4.3.2	$6110 \text{ BCE} \pm 40$
DSA17–04	KGM-IWd180341	Plant	2.57/1.13	$8300 \pm 50$	$-30.88 \pm 2.01$	$-646.86 \pm 2.01$	Oxcal v4.3.2	$6350 \text{ BCE} \pm 50$
DSE18–02	KGM-IWd180225	Plant	2.97/0.53	$210 \pm 30$	$-25.76 \pm 0.69$	$-34.25 \pm 3.70$	Oxcal v4.3.2	$1740 \text{ CE} \pm 30$
DSE18–02	KGM-IWd180226	Plant	5.74/–2.24	$7430 \pm 50$	$-26.49 \pm 0.39$	$-606.90 \pm 2.23$	Oxcal v4.3.2	$5480 \text{ BCE} \pm 50$
DSE18–03	KGM-IWd180320	Plant	3.85/–0.65	$1980 \pm 50$	$-34.29 \pm 2.58$	$-225.11 \pm 4.76$	Oxcal v4.3.2	$30 \text{ BCE} \pm 50$
DSE18–03	KGM-IWd180321	Plant	4.82/–1.62	$3530 \pm 50$	$-26.95 \pm 0.91$	$-360.91 \pm 4.15$	Oxcal v4.3.2	$1580 \text{ BCE} \pm 50$
DSE18–03	KGM-IWd180322	Plant	6.90/–3.70	$6290 \pm 40$	$-30.06 \pm 1.62$	$-546.59 \pm 2.34$	Oxcal v4.3.2	$4340 \text{ BCE} \pm 40$
DSE18–03	KGM-IWd180323	Plant	11.66/–8.46	$7300 \pm 40$	$-25.33 \pm 2.65$	$-600.32 \pm 2.09$	Oxcal v4.3.2	$5350 \text{ BCE} \pm 40$
DSE18–03	KGM-IWd180324	Plant	12.70/–9.50	$7390 \pm 40$	$-28.79 \pm 3.15$	$-604.90 \pm 2.13$	Oxcal v4.3.2	$5440 \text{ BCE} \pm 40$
DSE18–04	KGM-IWd180326	Plant	10.11/–7.71	$6850 \pm 40$	$-33.28 \pm 1.66$	$-577.32 \pm 2.30$	Oxcal v4.3.2	$4900 \text{ BCE} \pm 40$
DSE18–04	KGM-IWd180327	Plant	12.60/–10.20	$7350 \pm 40$	$-34.56 \pm 2.91$	$-602.67 \pm 2.16$	Oxcal v4.3.2	$5400 \text{ BCE} \pm 40$
DSE18–04	KGM-IWd180328	Plant	13.54/–11.14	$7650 \pm 40$	$-31.38 \pm 3.72$	$-617.19 \pm 2.11$	Oxcal v4.3.2	$5700 \text{ BCE} \pm 40$
DSE18–06	KGM-IWd180227	Plant	2.16/–0.96	Modern	$-28.86 \pm 0.26$	$44.78 \pm 3.98$	Oxcal v4.3.2	After 1950 CE
DSE18–06	KGM-IWd180337	Plant	3.06/–1.86	$90 \pm 30$	$-30.57 \pm 1.52$	$-18.68 \pm 3.63$	Oxcal v4.3.2	$1860 \text{ CE} \pm 30$
DSE18–06	KGM-IWd180228	Plant	3.95/–2.75	$2700 \pm 40$	$-26.98 \pm 0.30$	$-291.58 \pm 3.70$	Oxcal v4.3.2	$750 \text{ BCE} \pm 40$
DSE18–06	KGM-IWd180230	Plant	5.87/–4.67	$3910 \pm 40$	$-26.95 \pm 0.20$	$-390.25 \pm 3.00$	Oxcal v4.3.2	$1960 \text{ BCE} \pm 40$
DSE18–06	KGM-IWd180231	Plant	6.62/–5.42	$5000 \pm 60$	$-27.77 \pm 3.92$	$-467.76 \pm 4.16$	Oxcal v4.3.2	$3050 \text{ BCE} \pm 60$
DSE18–06	KGM-IWd180232	Plant	9.05/–7.85	$8020 \pm 80$	$-29.10 \pm 2.33$	$-634.43 \pm 3.54$	Oxcal v4.3.2	$6070 \text{ BCE} \pm 80$
DSE18–06	KGM-IWd180233	Plant	10.25/–9.05	$7940 \pm 70$	$-32.42 \pm 0.64$	$-630.72 \pm 3.12$	Oxcal v4.3.2	$5990 \text{ BCE} \pm 70$
DSE18–06	KGM-IWd180234	Plant	11.68/–10.48	$8070 \pm 50$	$-26.42 \pm 0.46$	$-636.60 \pm 2.19$	Oxcal v4.3.2	$6120 \text{ BCE} \pm 50$
DSE18–06	KGM-IWd180235	Plant	12.22/–11.02	$8080 \pm 40$	$-24.89 \pm 0.42$	$-637.49 \pm 1.97$	Oxcal v4.3.2	$6130 \text{ BCE} \pm 40$
DSE18–06	KGM-IWd180236	Plant	14.79/–13.59	$8250 \pm 50$	$-23.95 \pm 0.37$	$-644.99 \pm 2.01$	Oxcal v4.3.2	$6300 \text{ BCE} \pm 50$
DSE18–06	KGM-IWd180237	Plant	15.02/–13.82	$8360 \pm 50$	$-27.87 \pm 0.13$	$-649.48 \pm 2.04$	Oxcal v4.3.2	$6410 \text{ BCE} \pm 50$
DSE18–06	KGM-IWd180238	Plant	15.87/–14.67	$39,270 \pm 570$	$-31.04 \pm 0.51$	$-992.53 \pm 0.51$	Oxcal v4.3.2	$37320 \text{ BCE} \pm 570$
DSE18–06	KGM-IWd180239	Plant	16.73/–15.53	Over 53,671	$-28.75 \pm 0.54$	$-1000.56 \pm 0.17$	Oxcal v4.3.2	Over 50,000
DSE18–06	KGM-IWd180240	Plant	18.45/–17.25	$8240 \pm 50$	$-30.10 \pm 0.69$	$-644.45 \pm 2.32$	Oxcal v4.3.2	$6290 \text{ BCE} \pm 50$

**Table 2**  
OSL age dating results in the coastal area of Hwaseong City.

Borehole Name	OSL Sample Lab. No.	Water Content (%) <sup>a</sup>	Depth/Elevation (m)	Alpha dose (Gy/ka)	Beta dose (Gy/ka)	Gamma dose (Gy/ka)	Cosmic dose (Gy/ka)	Dose rate (Gy/ka)	D <sub>e</sub> (Gy)	Age (ka) (2σSE)
DS17-06	DS17-06 (170-175)	19.7 ± 5	1.73/2.17	0.37 ± 0.19	2.11 ± 0.13	1.14 ± 0.07	0.16 ± 0.01	3.78 ± 0.24	1.02 ± 0.02	0.27 ± 0.02
DS17-06	DS17-06 (250-255)	35.2 ± 5	2.53/1.37	0.33 ± 0.17	1.87 ± 0.11	1.04 ± 0.06	0.15 ± 0.01	3.38 ± 0.21	1.68 ± 0.06	0.50 ± 0.03
DS17-06	DS17-06 (330-335)	35.5 ± 5	3.33/0.57	0.33 ± 0.17	1.89 ± 0.11	1.06 ± 0.06	0.15 ± 0.01	3.43 ± 0.21	5.38 ± 0.07	1.57 ± 0.10
DS17-06	DS17-06 (430-435)	34.2 ± 5	4.33/-0.43	0.30 ± 0.15	1.81 ± 0.11	0.98 ± 0.05	0.12 ± 0.01	3.21 ± 0.19	20.60 ± 0.11	6.43 ± 0.39
DS17-06	DS17-06 (570-575)	36.3 ± 5	5.73/-1.83	0.34 ± 0.17	1.86 ± 0.11	1.05 ± 0.06	0.10 ± 0.01	3.35 ± 0.21	33.61 ± 0.40	10.00 ± 0.60
DS17-06	DS17-06 (640-645)	32.3 ± 5	6.43/-2.53	0.37 ± 0.19	1.12 ± 0.11	1.07 ± 0.06	0.09 ± 0.00	3.35 ± 0.22	35.56 ± 0.36	10.60 ± 0.70
DS17-06	DS17-06 (680-685)	15.4 ± 5	6.83/-2.93	0.26 ± 0.13	1.33 ± 0.10	0.73 ± 0.05	0.09 ± 0.00	2.41 ± 0.17	44.62 ± 0.66	18.50 ± 1.30
DS17-09	DS17-09 (280-285)	23.1 ± 5	2.83/4.24	0.41 ± 0.21	1.92 ± 0.12	1.13 ± 0.06	0.14 ± 0.01	3.60 ± 0.25	3.90 ± 0.16	1.08 ± 0.09
DS17-09	DS17-09 (320-325)	34.3 ± 5	3.23/3.84	0.39 ± 0.20	1.74 ± 0.10	1.08 ± 0.06	0.13 ± 0.01	3.34 ± 0.23	2.40 ± 0.02	0.72 ± 0.05
DS17-09	DS17-09 (380-385)	37.6 ± 5	3.83/3.25	0.31 ± 0.15	1.52 ± 0.09	0.89 ± 0.05	0.13 ± 0.01	2.84 ± 0.18	3.58 ± 0.06	1.26 ± 0.08
DSE18-06	DSE18-06 (230-235)	27.3 ± 5	2.33/-1.13	0.28 ± 0.14	1.97 ± 0.12	1.00 ± 0.06	0.15 ± 0.01	3.40 ± 0.19	1.51 ± 0.51	0.45 ± 0.15
DSE18-06	DSE18-06 (330-335)	31.2 ± 5	3.33/-2.13	0.37 ± 0.19	1.90 ± 0.11	1.11 ± 0.06	0.13 ± 0.01	3.52 ± 0.23	1.44 ± 0.40	0.41 ± 0.12
DSE18-06	DSE18-06 (480-485)	37.0 ± 5	4.83/-3.63	0.31 ± 0.16	1.76 ± 0.10	0.99 ± 0.05	0.11 ± 0.01	3.17 ± 0.19	0.43 ± 0.04	0.14 ± 0.02
DSE18-06	DSE18-06 (670-675)	36.7 ± 5	6.73/-5.53	0.33 ± 0.17	1.90 ± 0.11	1.05 ± 0.06	0.09 ± 0.00	3.36 ± 0.21	30.39 ± 0.11	9.03 ± 0.55
DSE18-06	DSE18-06 (750-755)	35.1 ± 5	7.53/-6.33	0.31 ± 0.16	1.84 ± 0.11	1.01 ± 0.05	0.08 ± 0.00	3.24 ± 0.20	30.69 ± 0.26	9.47 ± 0.58
DSE18-06	DSE18-06 (850-855)	38.3 ± 5	8.53/-7.33	0.31 ± 0.16	1.84 ± 0.10	1.01 ± 0.05	0.08 ± 0.00	3.24 ± 0.20	31.54 ± 0.30	9.74 ± 0.60
DSE18-06	DSE18-06 (950-955)	37.3 ± 5	9.53/-8.33	0.34 ± 0.17	1.90 ± 0.11	1.08 ± 0.06	0.07 ± 0.00	3.38 ± 0.21	30.86 ± 0.50	9.12 ± 0.59
DSE18-06	DSE18-06 (1240-1245)	33.7 ± 5	12.43/-11.23	0.34 ± 0.17	1.67 ± 0.10	0.98 ± 0.05	0.05 ± 0.00	3.04 ± 0.20	31.49 ± 0.36	10.37 ± 0.71

<sup>a</sup> The water content is expressed as the weight of water divided by the weight of dry sediments.

stimulation source and 0.140 Gys<sup>-1</sup> <sup>90</sup>Sr/<sup>90</sup>Y beta irradiation source. The single-aliquot regenerative dose (SAR) procedure (Murray and Wintle, 2000) was applied for equivalent dose (D<sub>e</sub>) determination. A preheating temperature of 220 °C for 10 s and a cut heat of 160 °C were selected. The sample was maintained at 125 °C during 100 s of stimulation with blue LEDs. The first 2 s of the OSL signal was used for D<sub>e</sub> calculations. Radionuclide contents were measured using low-level, high-resolution gamma spectrometry consisted of a Broad Energy Germanium detector (model BE6530; Canberra Industries, Meriden, CT, USA) and an ultra-low-background shield (model 777; Canberra Industries).

### 3.2. Grain size distribution

To confirm the change and distribution of the particle size characteristics of sediments, grain size analysis was performed on the collected sediment samples to confirm the grain size characteristics and distributions. To accurately analyze the grain size distribution of the collected samples, chemical pretreatment processes were performed. For the pretreated samples, grain size was measured using a laser particle analyzer (Mastersizer 3000; Malvern Instruments, Ltd., Worcestershire, UK) held by KIGAM. For the measured data, the particle size distribution characteristics were analyzed using the logarithmic graphical measures method of Folk and Ward (1957) using GRADISTAT Version 8.0 (Blott and Pye, 2001).

### 3.3. Diatom analysis

Diatoms were analyzed from 2.2 to 13.0 m from DSE18-06 core at 10–20 cm intervals, using around 0.1 g of dry sediment. Dry sediments

were placed into a 200 ml beaker with 5 ml of 30% hydrogen peroxide to remove organic matter. After boiling for 1 h, 200 ml of distilled water was poured into each beaker and samples were soaked for 4 h. Water was decanted and replaced twice with new distilled water. The additional distilled water was added thrice to separate substances and diatoms. Approximately 0.2–0.8 ml of the remaining solution from the bottom after decantation were pipetted onto a coverslip and mounted onto Mountmedia. At least 200 diatom valves were counted in each slide in the light microscope except for the depth from 6.5 to 8.5 m.

### 3.4. GIA model

We calculate RSL changes at selected locations in the study area during the Holocene using SELEN<sup>4</sup> (Spada and Melini, 2019), an open-source code that solves the sea level equation (Clark et al., 1978; Farrell and Clark, 1976; Peltier and Tushingham, 1989) governing how the global sea level changes through the melting of ice sheets and the solid Earth's time-dependent response to the ice and water mass redistribution, termed as the glacial isostatic adjustment (GIA). SELEN<sup>4</sup> requires an ice melting history that is associated with an assumed radial viscosity profile. Two out of the three combinations distributed with SELEN<sup>4</sup> are used in this study. These are the ice melting model ICE-5G based on the viscosity profile VM2r (Peltier, 2004) and ICE-6G based on VM5a (Peltier et al., 2015). SELEN<sup>4</sup> uses the present-day global topography model, ETOPO1 (Amante and Eakins, 2009; Eakins and Sharman, 2012) for calculating the lateral movement of shore lines. All the calculations were conducted on a Tegmark grid (Tegmark, 1996) with a resolution parameter of 44 corresponding to a uniform resolution of 46.31 km. All the fields were expanded by spherical harmonics up to the degree 476,

the maximum allowed on the chosen grid. We provide the complete set of input parameters and the list of the locations where RSL changes are calculated as supplementary information.

### 3.5. Sea-level indicator proxies

Based on the geomorphic and sedimentary characteristics and diatom analysis, the sedimentary environment of the study site was found to be primarily the tidal dominant estuaries (Dalrymple et al., 1992; Fan et al., 2013; Scanes et al., 2017) and the subtidal channels are generally flanked by intertidal and supratidal habitats of salt flats and salt marsh (Fig. 3 of Scanes et al., 2017). The relationships to the paleo-sea level of the basal peat and the salt marsh were applied to the peat proxy (Wang et al., 2013), and those of the intertidal zone and estuary sediments were also applied to each of the corresponding proxies in Table 4.

Recently the major maritime countries including the United States of America, Australia and the United Kingdom have adopted the lowest astronomical tide (LAT) and the highest astronomical tide (HAT) as the tidal datums. The LAT (HAT) values are, on average, 33.6 (46.2) cm lower (higher) than those of approximate lowest low water (approximate highest high water), ALLW (AHHW), along the west and south coast of Korea (Byun et al., 2019). The ALLW and the AHHW have been used as levels of tidal data for paleo-mean sea level (MSL) study in the Yellow Sea. Therefore, the current tide gauge data of Namyang Bay (National Geographic Institute, 1978), which is located 23 km south of the study site, was used to convert the dated layer into sea level index points (SLIPs) for comparing the results of recent papers on paleo-sea level in the Yellow Sea (Table 3). Estuarine sediments are thought to be accumulated above LAT; however, owing to the uncertainty that remains in the depth of deposition of estuarine/lagoon sediments, LAT are used as a conservative lower bound (Reynolds and Simms, 2015). In this study, LAT was replaced by LLW, although the former was 33.6 cm lower than the latter.

**Table 3**

Reference local tide gauges of Namyang and Incheon on the west coast of South Korea.

Water level (m)	Namyang Bay <sup>a</sup>	Water level (m)	Incheon <sup>b</sup>
Highest high water (HHW)	4.86	Highest astronomical tide (HAT)	5.10
Mean spring high water (MSHW)	4.16	Highest high water (HHW)	4.68
Mean high water (MHW)	3.13	(HAT-HHT)	0.42
Mean neap high water (MNHW)	2.10	Mean sea level (MSL)	0.00
Mean sea level (MSL)	0.13	Mean neap low water (MNLW)	
Mean neap low water (MNLW)	-1.85	Mean low water (MLW)	-2.88
Mean low water (MLW)	-2.88	(LAT-LLW)	-0.65
Mean spring low water (MSLW)	-3.91	Lowest low water (LLW)	-4.68
Lowest low water (LLW)	-4.61	Lowest astronomical tide (LAT)	-5.33

<sup>a</sup> National Geographic Institute (1978).

<sup>b</sup> Byun et al. (2019)

## 4. Results

### 4.1. Chronology and sedimentary facies

Overall sedimentary facies were classified based on <sup>14</sup>C and OSL age dating, grain size distribution, and diatom analysis results. Based on these results, the changes in the sedimentary environment in the Tando Estuary area were synthesized focusing on 2 cores (DS17-06 and DSE18-06) among 11 cores. The analysis results for each core from the salt marsh to the channel inlet are as follows. DS17-06 core site is the center of the salt marsh and the DSE18-06 core was collected at the tidal channel inlet.

Seven OSL dating results of 18.5–0.27 ka were identified for

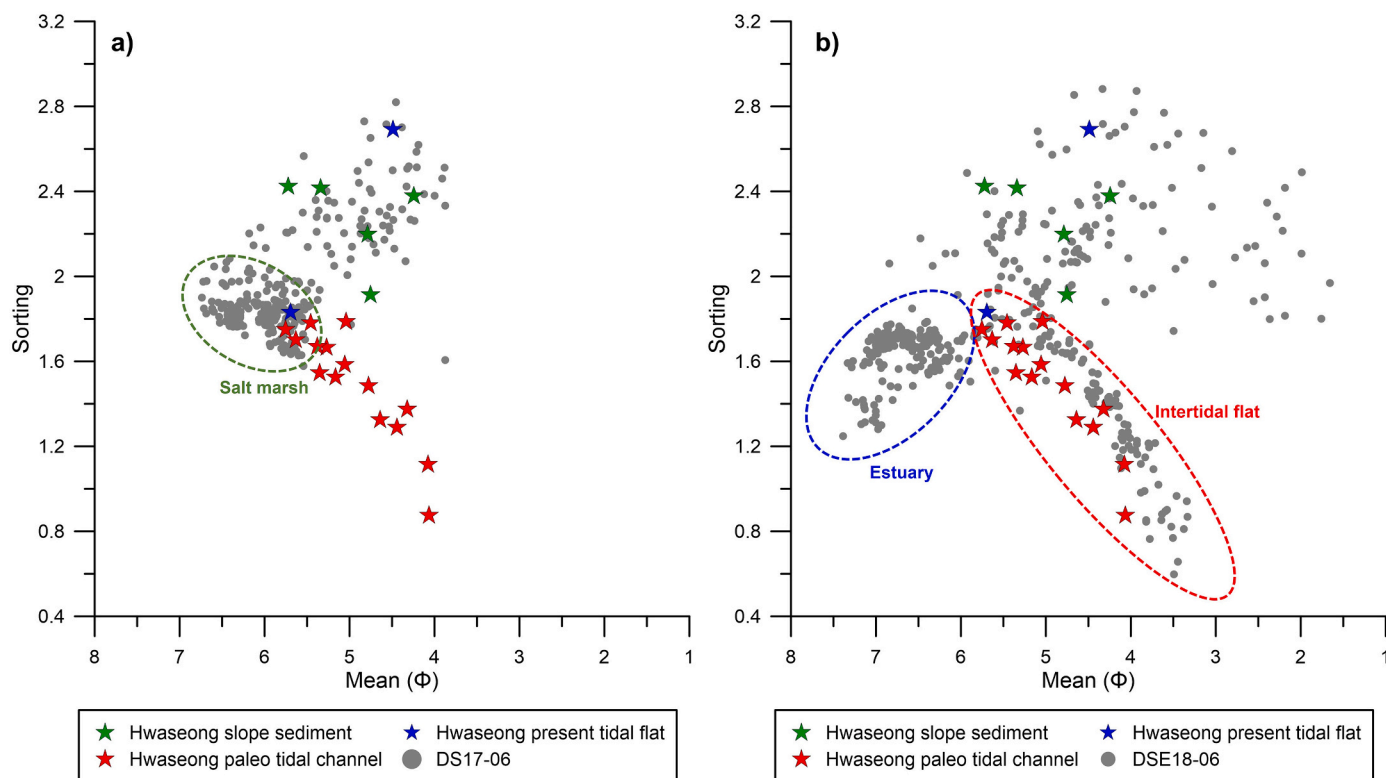


**Fig. 3.** Comparison of sediment grain size distribution (mean-sorting) between Hwaseong coast surface sample and cores. a) is the DS17-06 core, and b) is the DSE18-06 core.

sediment samples of DS17–06 core. The DS17–06 core sediments can be divided into the lower sand and gravel layer and the upper silt and sandy silt layers at the elevation  $-2.5$  m. The lower part is generally dark gray to black, and is estimated to change downward from the coarse sand layer to the sandy gravel layer. The sand and gravel sediments elevation of  $-4.1$  to  $-2.9$  m were estimated to be basal layer formed before 18.5 ka. This layer is estimated to be the basal sand and gravel sediment deposited during the Pleistocene, because the layer consisting of black sand and gravel coated with iron manganese oxide comes into contact with bedrock (Lim et al., 2003; Choi, 2005; Choi and Kim, 2006; Baek et al., 2017). Subsequently, a sand layer of 10.6 ka, about 35 cm thick, was unconformably overlain the basal sand and gravel layer. Also, the sand layer was covered with marine silt sediments. The layer contains a significant amount of sand patches over a thickness of approximately 1 m. The sandy silt layer was measured to be too old at about 10 ka, which may appear to be the effect of the sand patches from the lower layer, and is actually thought to be a layer deposited with the sea level rising after 8.2 ka. This layer was interpreted as estuary environment deposited in the early Holocene. Early Holocene silt sediments are considered to have been deposited in a relatively stable environment because of the small change in sand content even in a fast sea level rise environment (Dalrymple et al., 2003; Baek et al., 2017). If the sedimentary layer is too thin when considering the sedimentation period, it is inferred that the erosional activity was high or the sediment supply was low in various sedimentary environments. Sandy silt of 6.43 ka was overlain on it, after that the silt layer of 1.57 ka was deposited to a thickness of about 2 m. As such, it is thought that there is more than four unconformities due to erosion and interruption. This layer was interpreted as intertidal flat and salt marsh environment that developed in the upper intertidal zone deposited in the mid to late Holocene (Lim et al., 2003; Choi and Kim, 2006; Wang et al., 2013). The mid Holocene sand deposits, which have thin sediment thickness, are estimated to have been eroded several times in a relatively variable environment, resulting in unconformities with each of the lower and upper layers. In the upper part of the DS17–06 core, late Holocene deposits consist mainly of the sandy silt layer deposited approximately 500 years ago and the recent silt layer. This layer is interpreted as a salt marsh environment layer mixed with terrestrial sediments developing in the upper intertidal zone (Wang et al., 2013).

11 radiocarbon dates were determined for five plant slices (less than 5000 cal yr BP) and 6 plant roots (7940–8360 cal yr BP) from the DSE18–06 core. 5 OSL ages determined for samples from 6.7 to 12.4 m deep were older than 9 ka. Among the 5 OSL age results of DSE18–06, the age of 9.12 ka at  $-8.33$  a.m.s.l. was younger than those of  $-6.33$  and  $-7.33$  a.m.s.l., indicating an age reversal. The five OSL age outcomes between 9.03 and 10.36 ka were adjusted using trend lines from the age-elevation graph. The correction values (9.03, 9.12, 9.47, 9.74, 10.37 ka) were distributed within the error range of each age result, so it was estimated as a reasonable date. The age of the six plant roots of the DSE18–06 core between 7.9 and 8.4 cal kyr BP is almost constant and younger than the OSL age 8.7–10.6 ka between  $-5.5$  and  $-11.2$  m/ka respectively. This will indicate that the study area was also exposed during 7.9–8.4 ka under the influence of the 8.2 ka event. Based on these dating results, the early and late Holocene sedimentation rates were calculated to be 4.5 m/ka and 1.12 m/ka, respectively. Early Holocene sedimentation rates are much faster than late Holocene sedimentation rates.

Based on the organized age dating results, the chronology and sedimentary facies of the DSE18–06 core was classified. The DSE18–06 core sediments can be divided into Holocene and pre-Holocene (Pleistocene) deposits based on the basal peat layer (elevation  $-11.0$  to  $-11.2$  m). The basal peat layer overlain the gravel–sand–silt sediment layer at  $-11$  m a.m.s.l. Among the  $^{14}\text{C}$  dating results, the age confirmed through plant material excluding the root indicates an old age of 40–50 kyr BP or more. This layer was interpreted as an alluvial–fluvial environment deposited in the Pleistocene. The basal peat layer was identified as an

early Holocene sediment layer of approximately 10 ka. The characteristics of the sediment are sand containing a lot of silt, and substantial concentration of organic matter. This layer can be interpreted to be deposited in a temporary salt marsh environment with the onset of early Holocene marine transgression. Holocene deposits are further divided into early and mid to late Holocene deposits. Mid to late Holocene deposits are mainly composed of sand, and early Holocene deposits are mainly composed of silt and clay, with the shell-containing layer (elevation  $-4.05$  to  $-5.32$  m) as the boundary. On top of the basal peat layer, a silt layer of approximately 6 m thickness containing a lot of clay was deposited. That layer had age dating results of 9 to 10 ka, confirming that the sedimentation rate was very high. This layer was interpreted as estuary environment that was deposited with sea level rise during the early Holocene. The silt layer containing many gravel and shell fragments is located at an elevation of  $-4$  to  $-5$  m a.m.s.l. This layer can be interpreted as an environment in which tidal channels started to develop in a stabilized state after sea level rise in the mid Holocene. It is estimated that there were mid to late Holocene deposits at the top of the shell, so the existence of unconformity can be identified. In the upper part of the DSE18–06 core, relatively coarse silt and sand sedimentary layers are developed compared to the lower part. This layer was deposited hundreds of years ago in the late Holocene, and is characterized by a reversed age dating result. This means that the sedimentary environment is unstable, that is, it is located in the tidal channel, so it can be said that erosion and deposition were complicated by the change of the current path. The upper late Holocene layer is presumed to be deposited in the tidal channel of intertidal flat environment because the particle size is larger than the lower layer. Conversely, the lower early Holocene layer is estimated to be deposited in a stable environment in the estuary after the Holocene submergence owing to its small particle size and monotonous sedimentary facies.

#### 4.2. Grain size distribution

The results of grain size analysis of the core sediments (DS17–06 and DSE18–06) and the previously reported surface sediment from the Hwaseong coastal area (Han et al., 2017) were compared (Fig. 3). First, the surface sediment of the Hwaseong coast clearly distinguishes the tidal channel section, which agrees quite well with the intertidal flat channel section of DSE18–06 (Fig. 3b). In the case of the tidal channel, the tidal current velocity is rather fast even in a closed coast environment, so it is considered that the grain size is relatively large and the sorting is moderate. Such mean-sorting distribution can be said to represent the characteristics of the tidal channel that develops in the intertidal flat environment. Next, a section with a grain size of 5.5–7.5 phi and constant sorting is confirmed in the DSE18–06 core sediment, which is not confirmed on the surface of the Hwaseong coast. This can be estimated as estuarine environmental sediment, especially a lake or bay, deposited during a deep water depth after the Holocene submergence. Also, in the estuary environment, it can be seen that the grain size of the DSE18–06 core is smaller than that of the DS17–06, and the sorting of the DSE18–06 is better than DS17–06. Through this, it can be confirmed that the DSE18–06 core was placed in a deeper water level and a more stable sedimentary environment.

Second, there is very little overlap with the tidal channel between the Hwaseong coast sediment and the DS17–06 core (Fig. 3a). In the case of the surface slope sediment, it can be interpreted as the Pleistocene fluvial sediment of DS17–06. In the case of DS17–06 core, it means that the sedimentary environment was different from the current surface environment, and it can be estimated that it was the lake or bay environment of the Tando Estuary. Because the grain size is smaller than that of the surface sediment and the sorting is constant, it is interpreted that it was a more stable sedimentation environment. However, it can be seen that the mean-sorting distribution of DS17–06 core is different from that of DSE18–06. Regarding this, it is estimated that the grain size characteristics are different, because the location of the DS17–06 core is

far from the main tidal channel and is biased toward the land. Therefore, although it partially overlaps with the grain size distribution of the intertidal flat environment, it can be seen that it represents the result of the grain size distribution characteristic of the salt marsh environment.

#### 4.3. Diatom assemblage

Twenty diatom taxa were dominant in the DSE18–06 core (Fig. 4). The taxa reaching more than 10% relative abundance include *Actinocyclus senarius*, *Cyclotella stylonum*, *Paralia sulcata*, *Thalassionema nitzschioides*, *Thalassiosira* spp., *Diploneis smithii*, *Mastogloia* spp., *Nitzschia* spp., *Rhaphoneis surirella*, *Eunotia* spp., *Navicula* spp., *Pinnularia* spp. The taxa with relative abundance below 10% are *Cocconeis scutellum*, *Surirella fastuosa*, *Cymbella* spp., *Epithemia adnata*, *Gomphonema* spp., *Rhopalodia gibba*, *Stauroneis phoenicenteron*.

Below an elevation of  $-11.2$  m, the diatom does not occur. In the basal peat layer, at an elevation of  $-11.0$  to  $-11.2$  m, the dominant diatom species are *Enotia* spp. and *Pinnularia* spp., which prefer an acidic environment. Both diatoms are generally found in a swamp in Korea (Joh, 2012). The basal peat was developed during the late Pleistocene and Holocene when local groundwater levels rose in response to increasing RSL resulting in submerging the surface. Therefore, the basal peat could be used as an indicator of RSL rising (Denys and Baeteman, 1995). The groundwater dipped the core site as the RSL rose, and the environment changed to the swamp. In addition, marine diatom intermittently occurred in the basal peat layer (Fig. 4). It can support the assumption that the coastal line was closed to the coring site due to rising RSL.

Between elevation  $-11.0$  and  $-5.33$  m, the dominant species are *C. stylonum* and *Thalassiosira* spp. They are marine planktonic species and usually inhabit coastal environments (Lee and Park, 1997). In particular, *C. stylonum* and *T. nitzschioides* are an indicator of the input of oceanic water in the estuary environment (Sylvestre et al., 2004).

From elevation  $-5.33$  to  $-1.6$  m, *C. stylonum* abruptly decreased and *P. sulcata* increased. *Paralia sulcata* is normally observed in eutrophic coastal water (McQuoid and Nordberg, 2003). Increasing *P. sulcata* indicates the core site gets closer to the riverine environment because the enhanced nutrient results in the species booming.

#### 4.4. Estimating the paleo-MSL based on the sedimentary sea level proxy

Coastal sedimentary facies can be used as paleo-sea level proxies, based on the changes in the Holocene sedimentary environment (Chang et al., 1996; Fan et al., 2013; Song et al., 2013; Wang et al., 2013; Song et al., 2018). The diatom assemblage and sedimentary characteristics were used to identify the sedimentary sea-level proxies of the basal peat layer, estuarine channel, intertidal flats and salt marsh. RSL indicators, which have a definite relationship to past mean sea level (as described in section 3.5 and Table 4), are usually referred to as SLIPs. The indicative paleo-MSL are reconstructed based on such proxies (Table 5). The basal peat bed (Wang et al., 2013) and estuarine tidal flats (Reynolds and Simms, 2015) were used to establish the early Holocene mean sea level. In addition, although not the main subject of this paper, the mid- and late Holocene sea level data reconstructed from tidal flats and salt marsh sediments were added to Table 5 to compare the paleo-sea level behavior during the mid- and late Holocene between the study area and two sites of the Bohai Bay and Gunsan Bay. We suggested proxy types and the estimation processes of paleo-MSL at the indicative sedimentary boundaries in Table 4.

The basal peat bed in DSE18–06 core was confirmed at  $-11.23$  m in elevation at 10.37 ka. The paleo-MSL estimated from peat layer as a salt marsh is  $-14.88$  m using the relationship of mean spring high water (MSHW) - mean high water (MHW) of Table 4 (Chang et al., 1996; Wang et al., 2013). The corresponding basal peat layer is estimated to be located at  $(\text{MHW} + (\text{MSHW} - \text{MHW})/2) \pm (\text{MSHW} - \text{MHW})/2$  m higher than the paleo-MSL. That is, the paleo-MSL at that point is  $-11.23 - 3.65$

$\pm 0.52 = -14.88 \pm 0.52$  m. Unconformity was confirmed at  $-5.53$  m, the boundary between the estuary and intertidal flats. The upper boundary of the estuary in DSE18–06 is at  $-5.33$  m in elevation at 8.88 ka according to the linear relationship for the nearest two age data. The paleo-MSL at the upper boundary of the estuary can be estimated to be  $-3.82$  m at 8.88 ka using the relationship of mean sea level (MSL) - mean low water (MLW) of Table 4 (Reynolds and Simms, 2015). Estuary sediments are  $(\text{MSL} - \text{MLW})/2 \pm (\text{MSL} - \text{MLW})/2$  m lower than paleo-MSL, so paleo-MSL at the upper boundary of the estuary is converted to  $-3.82 \pm 1.51$  m. The elevation of the intertidal flats in DSE18–06 was confirmed between  $-5.33$  m at 4.3 ka and  $-1.6$  m at 2.9 ka, in which the distribution of oyster and shell fragments were identified. The range of the paleo-MSL estimated from the upper and lower boundaries of intertidal flats are  $-4.61 \pm 3.01$  m at 2.92 ka and  $-2.32 \pm 3.01$  m at 4.3 ka using the relationship of mean high water (MHW) - mean low water (MLW) of Table 4 (Chang et al., 1996; Wang et al., 2013).

In the DS17–06 core section ranging from an altitude of 2.6 to  $-1.1$  m, three sedimentary faces were confirmed. The intertidal flats with fine shell fragments distributed at an altitude of 1.9–0.9 m. This intertidal flat, which is underlain by a salt marsh layer (from 2.6 to 1.9 m above sea level), overlies the estuary sediments (from 0.9 to  $-1.1$  m above sea level). The paleo-MSL from the upper boundary of the intertidal flat is estimated as  $-1.1 \pm 3.01$  m at 0.35 ka (Chang et al., 1996; Wang et al., 2013) and that from the upper boundary of estuary is  $-0.61 \pm 1.51$  m at 7.6 ka using the meaning of MSL - MLW of Table 4 (Reynolds and Simms, 2015). We confirmed the distribution of organic matter in the from 2.6 to 1.9 m above sea level section of the DS17–06 and from 2.0 to 1.1 m above sea level section of the DSA17–04 core. These sections were confirmed to be marine sediments by diatom analysis.

Four cores of DS17–07 ( $-3.6$ – $-4.6$  m), DS17–14 ( $-3.4$ – $-4.3$  m), DSE18–03 ( $-9.3$ – $-9.6$  m) and DSE18–04 ( $-3.8$ – $-9.6$  m) have typical channel sediment characteristics. That is, they have an alternating sedimentary unit of silt and fine sand, often containing wood and rock fragments or gravels in the interval of each parenthesis. This phenomenon occurs intensively during 7.65–6.45 ka of the middle Holocene (Table 5).

#### 4.5. Model predictions for RSL changes at the study site

The calculated RSL changes at the location of core DSE18–06 since 11 ky BP are plotted in Fig. 5. The results based on the ice melting history model, ICE-6G, shows approximately  $-20$  m at around 11 ky BP. The RSL quasi-linearly rises up to approximately  $+5$  m by 6.5 ky BP, before decreasing to the present sea level (i.e., 0 m) at a much slower rate. The RSL variations based on ICE-5G follow the same pattern but remain consistently lower than the ICE-6G-based results.

## 5. Discussion

RSL records are lacking in far-field of the Pacific coast, particularly the Yellow Sea in Northeast Asia. There have been few research data indicating the beginning of the early Holocene transgression using basal peat on the east coast of the Yellow Sea. The early Holocene transgression data based on basal peat excavated from the study area will be of great significance in that it compares the beginning of transgression between the study site and other areas. SLIPs obtained from one study site during the Holocene could suggest reliable RSL change curve less affected by differences in sedimentation environment. Comparing this with the RSL change patterns in other study sites, such as Bohai Bay (Wang et al., 2020) and Gunsan Bay (Song et al., 2018), will be of decisive help in understanding transgression in the Yellow Sea during the early Holocene. There are two patterns of sea level rise in the study area: a rapid rise in the early Holocene Sea level (10–7.5 ka), and a high stand to 7.5–6 ka, followed by a gentle rise to 2 ka. Therefore, we attempted to compare the observed and the predicted the site's GIA

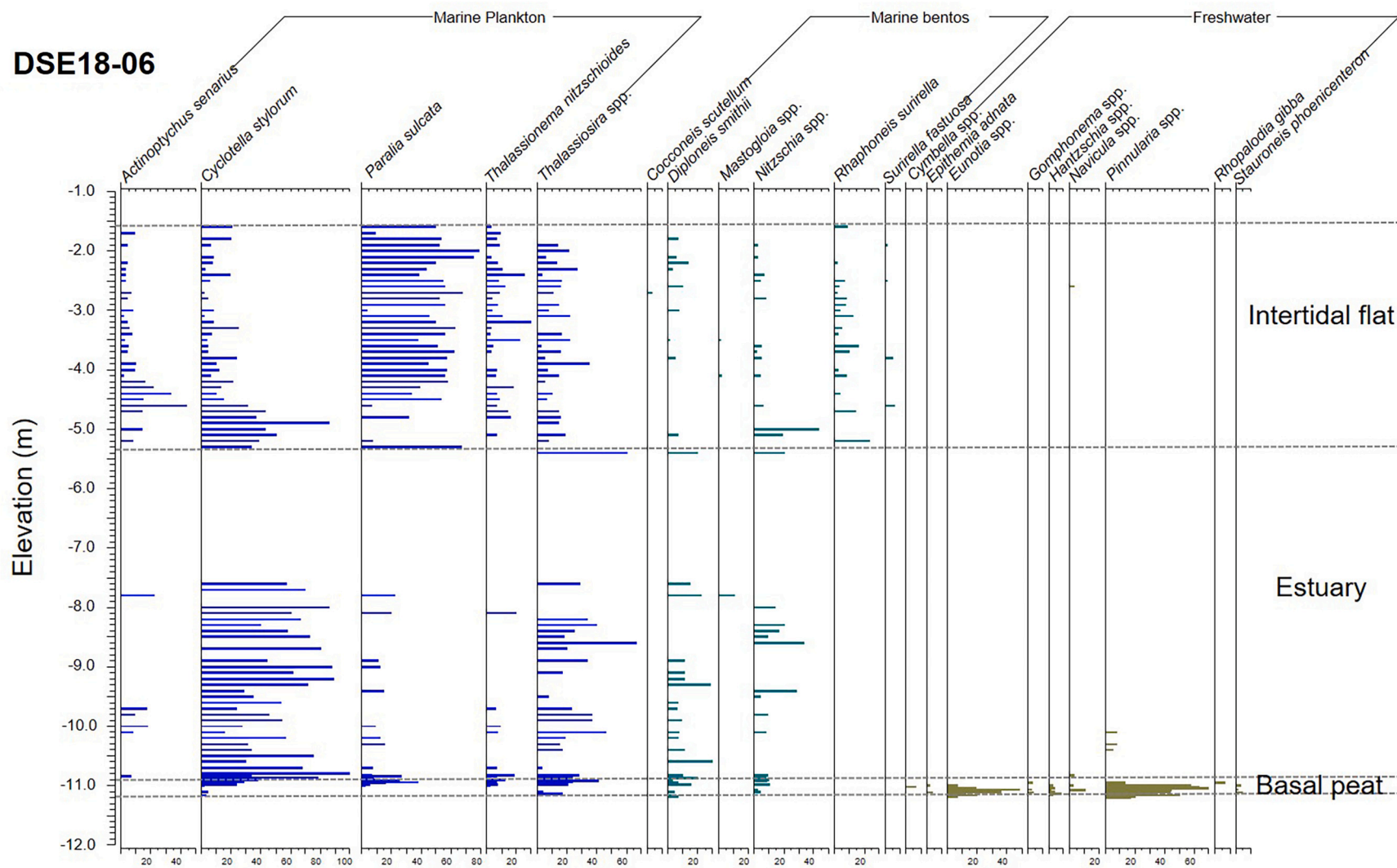


Fig. 4. Diatom assemblage results of DSE18-06 and comparison of sedimentary facies classification.

**Table 4**  
Proxy types and the estimation processes of paleo-MSL at the indicative sedimentary boundaries.

Borehole Name	sedimentary environment	Related proxy	Relationship to sea level	Altitude (m)	Error range (m)	Calibrated age (ka)	Paleo-MSL (m)
DSE18-06	Basal peat	Peat	MSHW-MHW <sup>1</sup>	-11.23	±0.52	10.37 ± 0.71	-14.88 ± 0.52 <sup>a</sup>
DSE18-06	Upper boundary of estuary	Estuary	MSL-MLW <sup>3</sup>	-5.33	±1.51	8.9*	-3.82 ± 1.51 <sup>b</sup>
DSE18-06	Lower boundary of intertidal flat	Tidal flat	MHW-MLW <sup>2</sup>	-5.33	±3.01	4.3*	-2.32 ± 3.01 <sup>c</sup>
DS17-13	Lower boundary of intertidal flat	Tidal flat	MHW-MLW <sup>2</sup>	-1.4	±3.01	3.6*	1.61 ± 3.01 <sup>d</sup>
DS17-13	Upper boundary of intertidal flat	Tidal flat	MHW-MLW <sup>2</sup>	1.6	±3.01	1.7*	-1.41 ± 3.01 <sup>e</sup>
DS17-06	Upper boundary of intertidal flat	Tidal flat	MHW-MLW <sup>2</sup>	1.9	±3.01	0.35*	-1.11 ± 3.01 <sup>f</sup>

<sup>1</sup> Wang et al., 2013

<sup>2</sup> Chang et al., 1996; Wang et al., 2013

<sup>3</sup> Reynolds and Simms, 2015

\* ages by extrapolation of two nearby points.

<sup>a</sup> -11.23 - (MHW+(MSHW-MHW)/2) ± (MSHW-MHW)/2.

<sup>b</sup> -5.33 + (MSL-MLW)/2 ± (MSL-MLW)/2.

<sup>c</sup> -5.33 + (MHW-MLW)/2 ± (MHW-MLW)/2.

<sup>d</sup> -1.4 + (MHW-MLW)/2 ± (MHW-MLW)/2.

<sup>e</sup> 1.6 - (MHW-MLW)/2 ± (MHW-MLW)/2.

<sup>f</sup> 1.9 - (MHW-MLW)/2 ± (MHW-MLW)/2.

model, discuss the differences between the site and the other two, and estimate the causes.

### 5.1. Comparison of the study site and other sites on the sedimentation environment and sea level rise rates in the early Holocene

Recently, a peat basal layer has been excavated from the Tando Estuary located on the mid-east coast of the Yellow Sea. This layer corresponds to the boundary between the pre-Holocene river sediments with a very high sand content and the marine sediments of clayey silts (Fig. 2). The basal peat layer is distributed at a thickness of 20 cm from -11.2 to -11.0 m of the DSE18-06 drilling core sediments. The deposit dated to approximately 10,296 yr BP is dominant in *Enotia* spp. and *Pinnularia* spp., which prefer an acid environment and is generally found in a swamp in Korea (Joh, 2012). The overlying layers provides information on the estuary or marine bay environment, dominated by marine plankton and marine benthic diatoms. The basal peat formation environment was estimated to be formed between mean spring high water (MSHW) and mean high water (MHW) (Chang et al., 1996; Wang et al., 2013). The paleo-mean sea level (paleo-MSL) estimated from the basal peat was -14.9 ± 0.52 m in depth at approximately 10,296 ± 400 yr BP (Table 2). Between 10.3 ka and 7.3 ka the paleo-MSL in the site rapidly rose from -14.9 to 0.45 m. The steep slope in the early Holocene obtained in the age-depth curve of the study area are based mainly on OSL age data (Fig. 5).

In addition, the differences in coastal types and tide ranges of the two sites of Tando Estuary and Bohai Bay can explain the early formation of the Tando Estuary even though it was relatively higher in elevation than Bohai Bay. As shown in Fig. 1b, Bohai Bay has a tide difference of 3–4 m while the study site has a wide tide difference of 8–9 m. Bohai Bay is an open coast, however the study site is a semi-enclosed coast. Therefore, the patterns of the pre-Holocene erosion and the early Holocene sedimentation are different in the two sites. In Bohai Bay, sediments were widely deposited mainly along the coastline; however, in the study site sediments were deposited through channels formed before and/or in the early Holocene, especially.

Conversely, Wang et al. (2020) reported that the oldest Holocene shoreline in Bohai Bay is, situated at -17.2 m at 9.7 ka cal BP. Between approximately 8.8 and 7.3 ka cal BP, the sea level rose rapidly from -15.4 to -7.0 m. The topographical elevation of the site is currently lower than that of Bohai Bay (Fig. 1b), but the RSL of the transgression of the early Holocene of Bohai Bay (9.7 ka cal BP; -17.2 m; Wang et al., 2020) was lower than that of the study site (10.3 ka cal BP; -13.7 m). The cause of these past and present reversal in coastal elevation may be explained by differences in the amount of sediment supplied under the

uncertainty of radiocarbon dating. A large amount of sediment from the Huanghe River has flowed into Bohai Bay (Wang et al., 2020).

The rate of sea level rise of the site in the early Holocene was 4.5 mm/y, slightly lower than 6.4 mm/y in Bohai Bay, but much lower than 14 mm/y in Gunsan Bay (Song et al., 2018), 140 km south of the study area. To explain this problem, it is necessary to introduce a GIA model that uses factors such as the earth surface viscosity and the sedimentary layer.

### 5.2. Comparison of the early Holocene sedimentation environment and sea level rise rate of Gunsan Bay and the study site

The west coast of Korea is a ria coast, and there are many large and small islands, and along the channels between them, tides flow into the coast, causing sedimentation and erosion. Unlike the study site, Gunsan Bay has a thick silt sedimentary layer under the influence of sediments flowing in along the Geum River Basin. Therefore, channel formation is active even in the coast affected by the tidal current. Therefore, compared to the study site, the thick silty sedimentary layers must have been deeply eroded and deposited before and during the Holocene.

The Gunsan Bay area studied by Song et al. (2018) was approximately 140 km south of the study area (Fig. 1c), and the Geum and Mangyeong Rivers flowed into it, and tidal flats developed at the estuaries of the two rivers. Gunsan Bay and the study site were compared for sedimentation environment and paleo-sea level rise. In the Gunsan area, the Holocene sedimentary facies were divided into three sedimentary units in ascending order, basement to tidal flat with silt in the early Holocene, marine transgression with sandy silt in middle Holocene, and tidal flat with silt in the late Holocene (Bak, 2015). The lowest indicative paleo-MSL of Gunsan Bay was -27.9 m at 9.8 ka, which was taken from the peat in lagoon (Song et al., 2018). This data must be from transgressions during the early Holocene. In the survey site, it appears at a depth of -13.7 m at 10.3 ka; hence, the elevation difference of the early Holocene transgression between the two regions is large.

Therefore, the transgression of Gunsan Bay must have started faster than that of the study site in the early Holocene. Also, when transgression started, sedimentation in the deep Gunsan Bay area should have taken place faster than that of the site. Hence, one of the conceivable reasons is the re-deposition after erosion of the initial sediment. Radiocarbon dating results are younger than one of OSL dating (Kim et al., 2015a; 2015b) should also be considered.

Conversely, since the age that determined the slope of the sea level fluctuation curve of the early Holocene of Tando Estuary was based on OSL data, there is no problem due to old carbon, etc. as in the dating using radiocarbon. In the early Holocene, the sea level rise rate in

**Table 5**  
Reconstruction of the indicative paleo-MSL based on the sedimentary sea-level proxy.

Borehole Name	Sedimentary environment	Elevation (m)	Age		Paleo-MSL (m)
			(ka, cal kyr BP)	Method	
<b>Early Holocene</b>					
DSE18-06	Basal peat	-11.23	10.37 ± 0.71	OSL	-14.88 ± 0.52
DSE18-06	Estuarine tidal flat	-8.33	9.12 ± 0.59	OSL	-6.83 ± 1.51
DSE18-06	Estuarine tidal flat	-7.33	9.74 ± 0.60	OSL	-5.83 ± 1.51
DSE18-06	Estuarine tidal flat	-6.33	9.47 ± 0.58	OSL	-4.83 ± 1.51
DSE18-06	Estuarine tidal flat	-5.53	9.03 ± 0.55	OSL	-4.03 ± 1.51
DSA17-04	Salt marsh (peat)	1.13	8.30 ± 0.05	<sup>14</sup> C	-1.99 ± 0.52
DSA17-04	Salt marsh (peat)	1.66	8.06 ± 0.05	<sup>14</sup> C	-2.52 ± 0.52
<b>Middle Holocene</b>					
DSE18-02	Low boundary of intertidal	-2.24	7.43 ± 0.05	<sup>14</sup> C	0.77 ± 3.01
DS17-13	Low boundary of intertidal	-2.56	7.28 ± 0.05	<sup>14</sup> C	0.45 ± 3.01
DS17-06	Intertidal flat	-0.43	6.43 ± 0.39	OSL	-0.43 ± 3.01
DSE18-03	Low boundary of intertidal	-3.70	6.29 ± 0.04	<sup>14</sup> C	-0.69 ± 3.01
<b>Late Holocene</b>					
DSE18-06	Intertidal flat	-4.67	3.91 ± 0.04	<sup>14</sup> C	-4.67 ± 3.01
DSE18-06	Estuarine tidal flat	-2.75	2.70 ± 0.04	<sup>14</sup> C	-1.24 ± 1.51
DSE18-03	Intertidal flat	-1.62	3.53 ± 0.05	<sup>14</sup> C	-1.62 ± 3.01
DS17-13	Intertidal flat	-1.20	2.90 ± 0.04	<sup>14</sup> C	-1.20 ± 3.01
DS17-13	Intertidal flat	-1.01	2.81 ± 0.04	<sup>14</sup> C	-1.01 ± 3.01
DSE18-03	Intertidal flat	-0.65	1.98 ± 0.05	<sup>14</sup> C	-0.65 ± 3.01
DS17-06	Salt marsh (peat)	1.37	0.50 ± 0.03	OSL	-2.28 ± 0.52
DS17-06	Salt marsh (peat)	2.17	0.27 ± 0.02	OSL	-1.48 ± 0.52
DSE18-02	Upper boundary of intertidal	0.53	0.21 ± 0.03	<sup>14</sup> C	-2.48 ± 3.01
<b>Estuarine channel deposits of middle Holocene</b>					
DSE18-04	Estuarine channel deposits	-11.14	7.65 ± 0.04	<sup>14</sup> C	-9.63 ± 1.51
DS17-07	Estuarine channel deposits	-4.63	7.49 ± 0.05	<sup>14</sup> C	-3.12 ± 1.51
DS17-07	Estuarine channel deposits	-4.38	7.43 ± 0.05	<sup>14</sup> C	-2.87 ± 1.51
DSE18-03	Estuarine channel deposits	-9.50	7.39 ± 0.04	<sup>14</sup> C	-7.99 ± 1.51
DSE18-04	Estuarine channel deposits	-10.20	7.35 ± 0.04	<sup>14</sup> C	-8.69 ± 1.51
DSE18-03	Estuarine channel deposits	-8.46	7.30 ± 0.04	<sup>14</sup> C	-6.95 ± 1.51
DSE18-04	Estuarine channel deposits	-7.71	6.85 ± 0.04	<sup>14</sup> C	-6.20 ± 1.51
DS17-14	Estuarine channel deposits	-3.85	6.45 ± 0.05	<sup>14</sup> C	-2.34 ± 1.51

Gunsan Bay was 14 mm/y (Song et al., 2018), which was much higher than the 4.5 mm/y in the study area and 6.4 mm/y in Bohai Bay (Wang et al., 2020). This is one of the possible evidences of sediments indicating the beginning of the early Holocene in Gunsan Bay which were

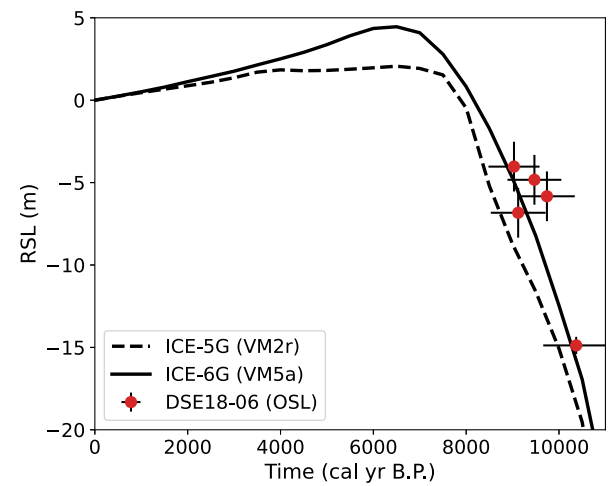


**Fig. 5.** Relative sea level (RSL) and OSL age data from the study site and two relative sea level changes at the location of DSE18-06 computed with SELEN<sup>4</sup> (Spada and Melini, 2019) based on ICE-6G (solid line) and ICE-5G (dashed line) glacial melting history models.

eroded and re-deposited. Further analysis using the GIA model is required.

### 5.3. Observed and predicted sea level

Since sedimentary mechanisms alone could not sufficiently explain the difference in sea level fluctuations in the early Holocene in the study area and in the Bohai Bay and Gunsan Bay, we compared our data with the GIA predictions. When the observation data are plotted together with the sea level predictions based on ICE 6G in the study area (Fig. 7), it can be seen that they are divided into two groups. The predictions and the observed data fit well during the early Holocene 10.3–8 ka, but during 8–7 ka the observed data are lower than the highest part of the prediction curve. The other group rises with a similar slope to the first group during 7.6–6 ka, but occurs 3–2 ka after the first group. It also rises gently during 4–2 ka and approaches the prediction curve at 2 ka. Coincidentally, the second group shows a similar pattern to the observation group in Bohai Bay (Fig. 7).

### 5.4. Comparison of the study site with other Yellow Sea sites

Song et al., 2018 presented the Holocene RSL curve for Gunsan Bay, mainly on the west coast of Korea. Subsequently, Wang et al. (2020) reconstructed the Holocene sea-level history of the northernmost China Sea shelf. Their observational data were compared with sea-level predictions obtained from global glacio-isostatic adjustment (GIA) models. The observed data for Gunsan Bay fit well with the predicted data, but the observed and the predicted data for Bohai Bay show some differences between them.

RSL reconstruction of Gunsan Bay (Song et al., 2018) is based on the Earth model with a lithospheric thickness of 96 km and two different upper and lower mantle viscosity parameters (Bradley et al., 2016), which we used to design models A and B. In model A, the upper and lower mantle viscosity parameters were specified as  $5 \times 10^{19}$  Pa s and  $10^{21}$  Pa s, respectively, while those in model B were specified as  $2 \times 10^{20}$  Pa s and  $8 \times 10^{21}$  Pa s, respectively (Bradley et al., 2016). Model A and Model B matched well with the SLIP extracted from the Gunsan region during 10–7 ka. However, it did not match well with the SLIP extracted from the study site (Fig. 6). It is estimated that sediments from the Gunsan area were deposited approximately 2 ka slower than the sediments from the study site in the early Holocene. These models are based on referring to the structural characteristics of southeastern China

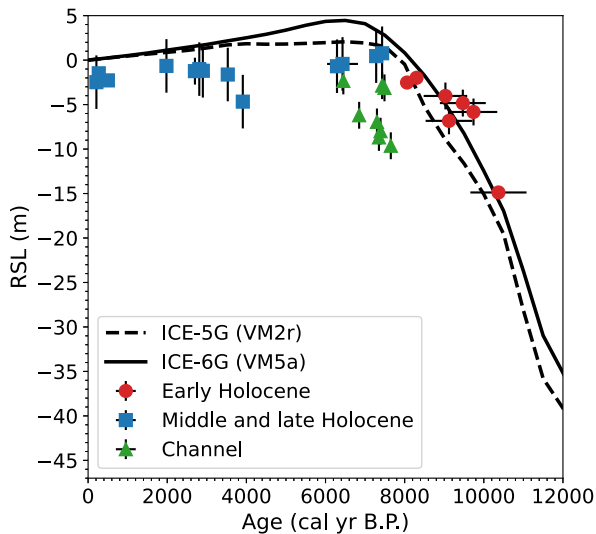


**Fig. 6.** a) Holocene RSL curves reconstructed by GIA modeling, the same with those shown in Fig. 5 and the Holocene RSL points reconstructed using paleo-MSL (Table 5) at the study site. b) The observed and the predicted Holocene RSL curves at Gunsan Bay modified from Song et al. (2018). In the study area and Gunsan Bay, 8.2 ka event was recognized at  $-1$  m and  $-6$  m, and the deepest SLIPs were indicated at  $-13.7$  m and  $-28$  m in elevation, respectively.

(Bradley et al., 2016). Considering one of the reasons why this model does not fit well with the data of the study site, it is presumed that the characteristics of the crust and sediments in the study site may be different from those of Gunsan and southeastern China. During the early Holocene, global temperatures rose rapidly, leading to significant ice sheet collapse, resulting in sea level rise during 10–8.5 cal kyr BP (Domack et al., 2001; North Greenland Ice Core Project members, 2004; Marcott et al., 2013). The rate of sea level rise then decreased during 8.4–7.8 cal kyr BP and the rate rose during 7.8–6.8 kyr BP (Song et al., 2018). They suggested that the sea level fluctuations on the west coast of Korea were synchronized with the sea level rise during 10 to 6.8 cal kyr BP. In addition, during the pre-Holocene in Gunsan, the sedimentary layer was thick and deep channels were formed due to river action. Even after transgression, the tidal current mainly passed through the channel, and deposition would have taken place preferentially. As the rate of sea level rise slowed, erosion and deposition would have been repeated in the channel. Therefore, it is thought that erosion and deposition were active in the study site from about 6–7.5 ka, and it is estimated that erosion and secondary deposition occurred preferentially along the past channel.

The Bohai Bay study by Wang et al. (2020) showed some differences between the observation data and the three GIA models. Wang et al. (2020) argued that the differences can be attributed to the two factors: (i) the age of the lowermost SLIP in core Q7 overestimated due to old carbon contamination of the dating material; (ii) the relatively shallow shoreline position in our study area being a deviation from eustasy due to the levering of the broad continental shelf in response to ocean load (e.g., Milne and Mitrović, 1998).

Conversely, the observation data of the study area were projected onto the prediction curve applied to the study of Bohai Bay. As observed from Fig. 7, the observation obtained during the early Holocene at the study site is in good agreement with the ICE 5G and ICE 6G curves among the GIA models of Bohai Bay. The data from the second group of the study site shows a pattern very similar to the observed in Bohai Bay, with some differences after 3 ka. However, the second pattern at the study site appears to be re-deposited in the channel during 8–6 ka. This is because sedimentation was dominant during the rapid sea level rise in the early Holocene, but then erosion and sedimentation would be

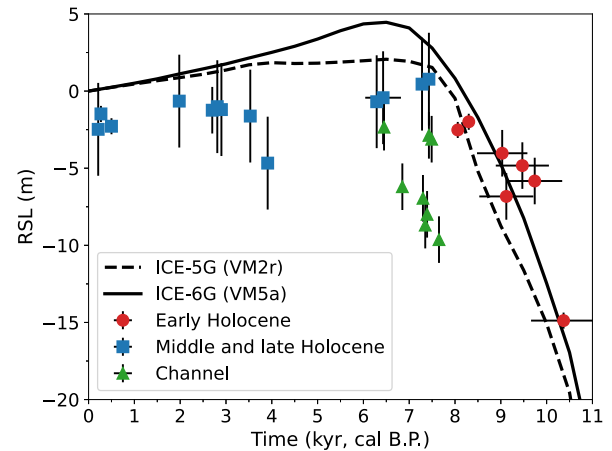


**Fig. 7.** The observed and the predicted RSL in a) the study site and b) the Bohai Bay. The RSL of the transgression of the early Holocene of Bohai Bay (9.7 cal kyr BP;  $-17.2$  m; Wang et al., 2018).

repeated as the rate slowed down.

In the Tando Estuary, the sea level rose rapidly during 10–8.3 ka. As mentioned in section 4.1, plant roots grew downward to a length of approximately 8 m during 8.0 to 8.3 ka. This is evidence that sea level rise has temporarily stopped and the bottom has been exposed. Moreover, the 8.2 ka cooling event has already been clearly recognized in the East Asian coast (Park et al., 2018, 2019). However, the depth at which this event occurs is approximately 5 m deeper in Gunsan Bay (Song et al., 2018) than at the study site. This difference suggests that, after sedimentation by transgression, the tectonic characteristics such as the viscosity of Gunsan Bay and the study site are different, so the levering effect is likely to be greater in the study area. However, the study area and Gunsan Bay are only 140 km away. Why can the tectonic characteristics be so different? As already described in section 2, the study area corresponds to the Gyeonggi Massif, and Gunsan area belongs to the Okcheon Metamorphic Zone (Koh et al., 2015; Liu and Zhou, 2019). Nd model age data currently support that the Gyeonggi massif and the Okcheon belt might have a close affinity to the Jiaobei terrane and the Sulu terrane in the North China Craton (Liu and Zhou, 2019). As shown in Fig. 1a, the Chugaryeong Fault Zone in the NNE–SSW direction passes through the Gunsan area, which is a tectonic-scale fault about 150 km long and 5–6 km wide (Choi et al., 2012). The northern part of Gunsan area corresponds to the west of the fault, and Quaternary activity of the fault has been reported in some areas of the fault system (Choi, 2011). Most of the areas that reached the high stand of sea-level in the mid-Holocene and gradually reached the current MSL are located in the northern part of Gunsan area on the east coast of the Yellow Sea (Choi, 2018). Conversely, the Bohai area is included in the North China Craton, and it is likely that there is a similarity between the Bohai and the study area.

Considering tectonic evidence, the levering effect after transgression in the early Holocene can be explained as similar to the study area and the Bohai area, but different from the Gunsan area. However, this will be a focus of a future study that needs to be addressed by obtaining more data.

## 6. Conclusions

The early Holocene RSL history of the study site were compared with those of Bohai Bay (the northernmost part of the study area) and Gunsan Bay (the southernmost point of the study area) on the Yellow Sea coast. A multi-proxy approach, including lithostratigraphy, biostratigraphy, combined with radiocarbon and OSL dating, facilitated generation of 28 paleo-sea level points reconstructed from 11 borehole sediments. The

observed RSL of the transgression in the early Holocene was  $-14.88$  m at 10.3 ka, which was much shallower than  $-27.9$  m in Gunsan Bay at 9.8 ka and was similar to  $-17.3$  m in Bohai Bay at 9.7 ka. We interpreted the cause of the paleo-RSL difference related to the early Holocene transgression that occurred at a similar period in the three regions, by examining the observed RSL and the predicted sea level change of the GIA model. The observed sea level index points in the early Holocene (10.3–8 ka) of the study area are in good agreement with the GIA prediction curves. The observed RSL and prediction curves of the study area were compared with those of other areas. In Gunsan Bay, the early Holocene GIA prediction curves are consistent with those observed, which seems to be the result of a “low setting” of the crust thickness and mantle viscosity when creating the GIA model. Therefore, it is presumed that the significant difference in the elevations observed between the study area and Gunsan Bay is caused by the levering effect owing to the difference in the tectonic characteristics. Conversely, the other groups observed during 7.6–6 ka show a slope similar to the prediction curve of the early Holocene in the study site, which is thought to be that the sediments of the early Holocene were eroded and re-deposited along the channels during the mid-Holocene.

### Declaration of Competing Interest

None.

### Acknowledgment

This work was supported by the Basic Research Project (GP2020-003) of the Korea Institute of Geoscience and Mineral Resource (KIGAM), Korean Ministry of Science and ICT.

### Appendix A. Supplementary data

Supplementary data to this article can be found online at <https://doi.org/10.1016/j.palaeo.2022.111185>.

### References

- Alexander, C.R., Nittrouer, C.A., Demaster, K.J., Park, Y.-A., Park, S.C., 1991. Macrotidal mudflats of the southwestern Korean coast; a model for interpretation of intertidal deposits. *J. Sediment. Petrol.* 61, 805–824. <https://doi.org/10.1306/D42677DA-2B26-11D7-8648000102C1865D>.
- Amante, C., Eakins, B.W., 2009. ETOPO1 Global Relief Model Converted to PanMap Layer Format. NOAA National Geophysical Data Center. PANGAEA. <https://doi.org/10.1594/PANGAEA.769615>.
- Baek, Y.S., Lee, S.H., Chang, T.S., 2017. Last interglacial to Holocene sedimentation on intertidal to subtidal flats revealed by seismic and deep-core sediment analyses, southwest coast of Korea. *Quat. Int.* 459, 45–54. <https://doi.org/10.1016/j.quaint.2017.08.001>.
- Bak, Y.S., 2015. Mid-Holocene Sea-level fluctuation inferred from diatom analysis from sediments on the west coast of Korea. *Quat. Int.* 384, 139–144. <https://doi.org/10.1016/j.quaint.2014.08.018>.
- Bloom, A.L., Park, Y.A., 1985. Holocene Sea-level history and tectonic movements, Republic of Korea. *Quat. Res.* 24, 77–84. <https://doi.org/10.4116/jaqua.24.77>.
- Blott, S.J., Pye, K., 2001. GRADISTAT: a grain size distribution and statistics package for the analysis of unconsolidated sediments. *Earth Surf. Process. Landf.* 26, 1237–1248. <https://doi.org/10.1002/esp.261>.
- Boyd, R., Dalrymple, R., Zaitlin, B., 1991. Evolutionary classification of coastal sediments. In: Shanley, K.W., Perkins, B.F. (Eds.), *Coastal Depositional Systems in the Gulf of Mexico: Quaternary Framework and Environmental Issues*. SEPM Society for Sedimentary Geology, 12. <https://doi.org/10.5724/gcs.91.12.0030>.
- Bradley, S.L., Milne, G.A., Horton, B.P., Zong, Y., 2016. Modelling Sea level data from China and Malay-Thailand to estimate Holocene ice-volume equivalent sea level change. *Quat. Sci. Rev.* 137, 54–68. <https://doi.org/10.1016/j.quascirev.2016.02.002>.
- Byun, D.S., Choi, B.J., Kim, H., 2019. Estimation of the lowest and highest astronomical tides along the west and south coast of Korea from 1999 to 2017. *J. Korean Soc. Oceanogr.* 24, 495–508. <https://doi.org/10.7850/jkso.2019.24.4.495>.
- Chang, K.H., 2013. Middle Paleozoic sedimentary province within Sino-Korean Plate: Paleogeographic implication for Okcheon metamorphic zone. *J. Geol. Soc. Korea* 49, 437–452. <https://doi.org/10.14770/jgsk.2013.49.4.437>.
- Chang, J.H., Choi, J.Y., 2001. Tidal-flat sequence controlled by Holocene Sea-Level rise in Gomsu Bay, West Coast of Korea. *Estuar. Coast. Shelf Sci.* 52, 391–399. <https://doi.org/10.1006/ecss.2000.0745>.
- Chang, J.H., Park, Y.A., Han, S.J., 1996. Late Quaternary stratigraphy and sea-level change in the tidal flat of Gomsu Bay, west coast of Korea. *J. Korean Soc. Oceanogr.* 1, 59–72.
- Chang, T.S., Kim, S.P., Yoo, D.G., Lee, E., 2011. Is the mid-channel tidal bar a potential hazard for shipping in a narrow macrotidal seaway of outer Asan Bay, Korea? *J. Coast. Res.* S164, 880–884. <https://www.jstor.org/stable/26482299>.
- Choi, K., 2005. Pedogenesis of late Quaternary deposits, northern Kyonggi Bay, Korea: Implications for relative sea-level change and regional stratigraphic correlation. *Palaeogeogr. Palaeoclimatol. Palaeoecol.* 220 (3–4), 387–404. <https://doi.org/10.1016/j.palaeo.2005.02.006>.
- Choi, S.J., 2011. Active fault map and seismic hazard map. *J. Disaster Prev.* 13, 161–162.
- Choi, S.J., 2018. Review on the relative sea-level changes in the Yellow Sea during the late Holocene. *Econ. Environ. Geol.* 51, 463–471. <https://doi.org/10.9719/EEG.2018.51.5.463>.
- Choi, K., Kim, S.-P., 2006. Late Quaternary evolution of macrotidal Kimpo tidal flat, Kyonggi Bay, west coast of Korea. *Mar. Geol.* 232 (1–2), 17–34. <https://doi.org/10.1016/j.margeo.2006.06.007>.
- Choi, S.J., Chwae, U.C., Lee, H.K., Song, Y.G., Kang, I.M., 2012. Review on Chugaryeong fault. *Econ. Environ. Geol.* 45, 441–446. <https://doi.org/10.9719/EEG.2012.45.4.441>.
- Chough, S.K., 2013. Geology and Sedimentary of the Korean Peninsula. Elsevier, Amsterdam. <https://doi.org/10.1016/C2012-0-02847-5>.
- Chough, S.K., Lee, H.J., Yoon, S.H., 2000. Marine Geology of Korean Seas. Elsevier, Amsterdam.
- Chough, S.K., Lee, H.J., Chun, S.S., Shinn, Y.J., 2004. Depositional processes of late Quaternary sediments in the Yellow Sea: a review. *Geosci. J.* 8, 211–264. <https://doi.org/10.1007/BF02910197>.
- Clark, J.A., Farrell, W.E., Peltier, W.R., 1978. Global changes in Postglacial Sea Level: a numerical calculation. *Quat. Res.* 9, 265–287. [https://doi.org/10.1016/0033-5894\(78\)90033-9](https://doi.org/10.1016/0033-5894(78)90033-9).
- Cummings, D.I., Dalrymple, R.W., Choi, K., Jin, J.H., 2015. The Tide-Dominated Han River Delta, Korea. Elsevier, Amsterdam. <https://doi.org/10.1016/C2013-0-15362-7>.
- Dalrymple, R.W., Zaitlin, B.A., Boyd, R., 1992. Estuarine facies models; conceptual basis and stratigraphic implications. *J. Sediment. Res.* 62 (6), 1130–1146. <https://doi.org/10.1306/D4267A69-2B26-11D7-8648000102C1865D>.
- Dalrymple, R.W., Baker, E.K., Harris, P.T., Hughes, M.G., 2003. Sedimentology and stratigraphy of a tide-dominated foreland-basin delta (Fly River, Papua New Guinea). In: Sidi, F.H., Nummedal, D., Imbert, P., Darman, H., Posamentier, H.W. (Eds.), *Tropical Deltas of Southeast Asia—Sedimentology, Stratigraphy, and Petroleum Geology*. SEPM, pp. 147–173 (Special Publication 76).
- Denys, L., Baeteman, C., 1995. Holocene evolution of relative sea-level and local mean high water spring tides in Belgium—a first assessment. *Mar. Geol.* 124, 1–19. [https://doi.org/10.1016/0025-3227\(95\)00029-X](https://doi.org/10.1016/0025-3227(95)00029-X).
- Domack, E., Leventer, A., Dunbar, R., Taylor, F., Brachfeld, S., Sjunneskog, C., ODP Leg 178 Scientific Party, 2001. Chronology of the Palmer deep site, Antarctic Peninsula: a Holocene palaeoenvironmental reference for the circum-Antarctic. *Holocene* 11, 1–9. <https://doi.org/10.1191/095968301673881493>.
- Eakins, B.W., Sharman, G.F., 2012. Hypsographic Curve of Earth’s Surface from ETOPO1, 5. NOAA National Geophysical Data Center, Boulder, CO, p. 1.
- Fan, D., Yuan, W., Min, L., 2013. Classifications, sedimentary features and facies associations of tidal flats. *J. Palaeogeogr.* 2, 66–80. <https://doi.org/10.3724/SP.J.1261.2013.00018>.
- Farrell, W.E., Clark, J.A., 1976. On Postglacial Sea level. *Geophys. J. Int.* 46, 647–667. <https://doi.org/10.1111/j.1365-246X.1976.tb01252.x>.
- Folk, R.L., Ward, W.C., 1957. Brazos River bar: a study in the significance of grain size parameters. *J. Sediment. Petrol.* 27, 3–26. <https://doi.org/10.1306/74D70646-2B21-11D7-8648000102C1865D>.
- Han, M., Yang, D.Y., Lim, J., 2017. Basic research of the paleo-environmental change and possibility of ancient port location through geomorphological survey and sediment analysis in Hwaseong City. *J. Korean Geomorphol. Assoc.* 24, 27–41. <https://doi.org/10.16968/JKGA.24.4.27>.
- International Hydrographic Organization, 1953. *Limits of Oceans and Seas*. 3rd edition, Special Publication No. 23. International Hydrographic Organization, Monaco.
- Jin, J.H., Chough, S.K., Ryang, W.H., 2002. Sequence aggradation and systems tracts partitioning in the mid-eastern Yellow Sea: roles of glacio-eustasy, subsidence and tidal dynamics. *Mar. Geol.* 184, 249–271. [https://doi.org/10.1016/S0025-3227\(01\)00281-X](https://doi.org/10.1016/S0025-3227(01)00281-X).
- Joh, G.J., 2012. *Algal Flora of Korea Volume 3 Number 7 Freshwater Diatoms V*. National Institute of Biological Resource, Incheon, p. 132.
- Jung, T.S., 2014. Change of mean Sea Level due to coastal development and climate change in the Western Coast of Korean Peninsula. *J. Ocean Eng. Technol.* 26, 120–130. <https://doi.org/10.9765/KSCOE.2014.26.3.120>.
- Kim, Y.H., Lee, H.J., Chun, S.S., Han, S.J., Chough, S.K., 1999. Holocene transgressive stratigraphy of a macrotidal flat in the southeastern Yellow Sea: Gomsu Bay, Korea. *J. Sediment. Res.* 69, 328–337. <https://doi.org/10.2110/jsr.69.328>.
- Kim, J.C., Chang, T.S., Yi, S., Hong, S.S., Nahm, W.H., 2015a. OSL dating of coastal sediments from the south-western Korean Peninsula: a comparison of different size fractions of quartz. *Quat. Int.* 384, 82–90. <https://doi.org/10.1016/j.quaint.2014.09.001>.
- Kim, J.C., Cheong, D., Shin, S., Park, Y.H., Hong, S.S., 2015b. OSL chronology and accumulation rate of the Nakdong deltaic sediments, southeastern Korean Peninsula. *Quat. Geochronol.* 30, 245–250. <https://doi.org/10.1016/j.quageo.2015.01.006>.
- Kim, J.C., Yoo, D.G., Hong, S.H., Yoon, Y.H., Shin, S., Han, M., Choi, J., Cheong, D., Lee, J.-Y., Choi, H., 2021. Chronostratigraphic and palaeogeographic interpretation of Nakdong deltaic sequences in the south-eastern Korean Peninsula. *Palaeogeogr.*

- Palaeoclimatol. Palaeoecol. 584, 110654 <https://doi.org/10.1016/j.palaeo.2021.110654>.
- Koh, H.J., Ko, K., Kwon, C.W., Kee, W.S., Kim, B.C., Kim, S.W., Kim, Y.B., Kim, Y.H., Kim, H.C., Park, S.I., Song, K.Y., Yeon, Y.K., Lee, S.R., Lee, S.S., Lee, S.R., Lee, S.B., Lee, H.J., Cho, D.R., Chi, K.H., Choi, S.J., Choi, B.Y., Hwan, J.K., Hwang, J.H., Hyeon, H.J., Hong, B., Jeon, H.Y., Kim, Y.S., Roh, J.R., Kang, K.H., 2015. Tectonostratigraphy of the Mid-West Korean Peninsula and Construction of the Integrated Geoscience Information System. Basic Research Report of the Korea Institute of Geoscience and Mineral Resources (243 pp).
- Korea Ocean Research and Development Institute, 1994. Quaternary Sea-Level Changes and Their Implication in the Evolution of Coastal Depositional Environments (III). Seoul, Korea, Korea Ocean Research and Development Institute, Report BSPN 00223-732-5 (315 pp).
- Lambeck, K., Smither, C., Johnston, P., 1998. Sea-level change, glacial rebound and mantle viscosity for northern Europe. *Geophys. J. Int.* 134, 102–144. <https://doi.org/10.1046/j.1365-246x.1998.00541.x>.
- Lee, E., Chang, T.S., 2015. Holocene Sea level changes in the Eastern Yellow Sea: a brief review using proxy records and measurement data. *J. Korean Earth Sci. Soc.* 36, 520–532. <https://doi.org/10.5467/JKESS.2015.36.6.520>.
- Lee, H.J., Chu, Y.S., 2001. Origin of inner-shelf mud deposit in the Southeastern Yellow Sea: Huksan Mud Belt. *J. Sediment. Res.* 71, 144–154. <https://doi.org/10.1306/040700710144>.
- Lee, Y.G., Park, Y.A., 1997. Stratigraphy, sedimentary facies and diatoms of the tidal sediments in Hampyeong Bay, West Coast of Korea. *J. Korean Earth Sci. Soc.* 18, 90–98.
- Lim, D.I., Choi, J.Y., Jung, H.S., 2003. Characteristics and stratigraphy of late Quaternary sediments on a macrotidal mudflat deposit of Namyang Bay, western coast of Korea. *J. Korean Earth Sci. Soc.* 24, 46–60.
- Lim, D.I., Choi, J.Y., Jung, H.S., Rho, K.C., Ahn, K.S., 2007. Recent sediment accumulation and origin of shelf mud deposits in the Yellow and East China Seas. *Prog. Oceanogr.* 73 (2), 145–159. <https://doi.org/10.1016/j.pocan.2007.02.004>.
- Liu, F., Zhou, Y., 2019. Nd isotopic and model age study of the Shandong Province, North China Craton: Implications for correlation with South Korea. *J. Earth Sci.* 30, 938–951. <https://doi.org/10.1007/s12583-019-1213-1>.
- Liu, Z., Hu, D., Tang, X., Wei, E., 2007. Rotary spectrum analysis of tidal current in the southern Yellow Sea. *Chin. J. Oceanol. Limnol.* 25, 286–291. <https://doi.org/10.1007/s00343-007-0286-3>.
- Lowe, J.A., Bernie, D., Bett, P., Bricheno, L., Brown, S., Calvert, D., Clark, R., Eagle, K., Edwards, T., Fossier, G., Fung, F., Gohar, L., Good, P., Gregory, J., Harris, G., Howard, T., Kaye, N., Kendon, E., Krijnen, J., Maisey, P., McDonald, R., McInnes, R., McSweeney, C., Mitchell, J.F.B., Murphy, J., Palmer, M., Roberts, C., Rostron, J., Sexton, D., Thornton, H., Tinker, J., Tucker, S., Yamazaki, K., Belcher, S., 2018. UKCP18 Science Overview Report (73p).
- Marcott, S.A., Shakun, J.D., Clark, P.U., Mix, A.C., 2013. A reconstruction of regional and global temperature for the past 11,300 years. *Science*. 339, 1198–1201. <https://doi.org/10.1126/science.1228026>.
- McQuoid, M.R., Nordberg, K., 2003. The diatom *Paralia sulcata* as an environmental indicator species in coastal sediments. *Estuar. Coast. Shelf Sci.* 56, 339–354. [https://doi.org/10.1016/S0272-7714\(02\)00187-7](https://doi.org/10.1016/S0272-7714(02)00187-7).
- Meijles, E.W., Kiden, P., Streurman, H.J., van der Plicht, J., Vos, P.C., Ghehrels, W.R., Kopp, R.E., 2018. Holocene relative mean sea-level changes in the Wadden Sea area, northern Netherlands. *J. Quat. Sci.* 33, 905–923. <https://doi.org/10.1002/jqs.3068>.
- Milliman, J.D., Syvitski, J.P., 1992. Geomorphic/tectonic control of sediment discharge to the ocean: the importance of small mountainous rivers. *J. Geol.* 100 (5), 525–544. <https://doi.org/10.1086/629606>.
- Milne, G.A., Mitrovica, J.X., 1998. Postglacial Sea-level change on a rotating Earth. *Geophys. J. Int.* 133, 1–19. <https://doi.org/10.1046/j.1365-246x.1998.1331455.x>.
- Murray, A.S., Wintle, A.G., 2000. Luminescence dating of quartz using an improved single-aliquot regenerative-dose protocol. *Radiat. Meas.* 32, 57–73. [https://doi.org/10.1016/S1350-4487\(99\)00253-X](https://doi.org/10.1016/S1350-4487(99)00253-X).
- Nahm, W.H., Hong, S.S., 2014. Holocene environmental changes inferred from sedimentary records in the lower reach of the Yeongsan River, Korea. *Holocene*. 24, 1798–1809. <https://doi.org/10.1177/0959683614551221>.
- National Geographic Institute, 1978. Basic Research Report on Nearshore Environments of Korea (Asan Bay and Adjacent Areas). Seoul (63p).
- North Greenland Ice Core Project members, 2004. High-resolution record of Northern Hemisphere climate extending into the last interglacial period. *Nature*. 431, 147–151. <https://doi.org/10.1038/nature02805>.
- Park, S.C., Lee, S.D., 1994. Depositional patterns of sand ridges in tidal-dominated shallow water environments: Yellow Sea Coast and South Sea of Korea. *Mar. Geol.* 120, 89–103. [https://doi.org/10.1016/0025-3227\(94\)90079-5](https://doi.org/10.1016/0025-3227(94)90079-5).
- Park, J.H., Yi, S., Oh, H., Xue, B., 2015. Holocene shoreline displacement on the Gungnam Plain, Buyeo, near the central west coast of South Korea inferred from diatom assemblages. *Quat. Int.* 384, 129–138. <https://doi.org/10.1016/j.quaint.2015.04.046>.
- Park, J., Park, J., Yi, S., Kim, J.C., Lee, E., Jin, Q., 2018. The 8.2 ka cooling event in coastal East Asia: High-resolution pollen evidence from southwestern Korea. *Sci. Rep.* 8, 12423. <https://doi.org/10.1038/s41598-018-31002-7>.
- Park, J., Park, J., Yi, S., Kim, J.C., Lee, E., Choi, J., 2019. Abrupt Holocene climate shifts in coastal East Asia, including the 8.2 ka, 4.2 ka, and 2.8 ka BP events, and societal responses on the Korean peninsula. *Sci. Rep.* 9, 10806. <https://doi.org/10.1038/s41598-019-47264-8>.
- Peltier, W.R., 2004. Global glacial isostasy and the surface of the ICE-age Earth: the ICE-5G (VM2) model and GRACE. *Annu. Rev. Earth Planet. Sci.* 32, 111–149. <https://doi.org/10.1146/annurev.earth.32.082503.144359>.
- Peltier, W.R., Tushingham, A.M., 1989. Global Sea level rise and the greenhouse effect: might they be connected? *Science*. 244, 806–810. <https://doi.org/10.1126/science.244.4906.806>.
- Peltier, W.R., Argus, D.F., Drummond, R., 2015. Space geodesy constrains ICE age terminal deglaciation: the global ICE-6G C (VM5a) model. *J. Geophys. Res. Solid Earth* 120, 450–487. <https://doi.org/10.1002/2014JB011176>.
- Ramsey, C.B., 2017. Methods for summarizing radiocarbon datasets. *Radiocarbon* 59, 1809–1833. <https://doi.org/10.1017/RDC.2017.108>.
- Reimer, P.J., Bard, E., Bayliss, A., Beck, J.W., Blackwell, P.G., Ramsey, C.B., Buck, C.E., Cheng, H., Edwards, R.L., Friedrich, R.M., Grootes, P.M., Guilderson, T.P., Hafliadason, H., Hajdas, I., Hatté, C., Heaton, T.J., Hoffmann, D.L., Hogg, A.G., Hughen, K.A., Kaiser, K.F., Kromer, B., Manning, S.W., Niu, M., Reimer, R.W., Richards, D.A., Scott, E.M., Southon, J.R., Staff, R.A., Turney, C.S.M., van der Plicht, J., 2013. Intcal13 and Marine13 radiocarbon age calibration curves 0–50,000 years cal BP. *Radiocarbon* 55, 1869–1887. [https://doi.org/10.2458/azu\\_rc.55.16947](https://doi.org/10.2458/azu_rc.55.16947).
- Reynolds, L.C., Simms, A.R., 2015. Late Quaternary relative sea level in Southern California and Monterey Bay. *Quat. Sci. Rev.* 126, 57–66. <https://doi.org/10.1016/j.quascirev.2015.08.003>.
- Scanes, P., Ferguson, A., Potts, J., 2017. Estuary form and function; implications for Paleoenvironmental studies. In: Weckström, K., Saunders, K.M., Gell, P.A., Skilbeck, C.G. (Eds.), *Applications of Paleoenvironmental Techniques in Estuarine Studies. Part of the Developments in Paleoenvironmental Research book series (DPER, volume 20)*. Springer, pp. 9–44. [https://doi.org/10.1007/978-94-024-0990-1\\_2](https://doi.org/10.1007/978-94-024-0990-1_2).
- Shinn, Y.J., Chough, S.K., Kim, J.W., Woo, J., 2007. Development of depositional systems in the southeastern Yellow Sea during the postglacial transgression. *Mar. Geol.* 239, 59–82. <https://doi.org/10.1016/j.margeo.2006.12.007>.
- Simpson, M.J.R., Ravnald, O.R., Sande, H., Nilsen, J.E.Ø., Kierulf, H.P., Vestøl, O., Steffen, H., 2017. Projected 21st century sea-level changes, observed sea level extremes, and sea level allowances for Norway. *J. Mar. Sci. Eng.* 5, 36. <https://doi.org/10.3390/jmse5030036>.
- Song, B., Li, Z., Saito, Y., Okuno, J., Li, Z., Lu, A., Hua, D., Li, J., Li, Y., Nakashima, R., 2013. Initiation of the Changjiang (Yangtze) delta and its response to the mid-Holocene Sea level change. *Palaeogeogr. Palaeoclimatol. Palaeoecol.* 388, 81–97. <https://doi.org/10.1016/j.palaeo.2013.07.026>.
- Song, B., Yi, S., Yu, S.Y., Nahm, W.H., Lee, J.Y., Lim, J., Kim, J.C., Yang, Z., Han, M., Jo, K.N., Saito, Y., 2018. Holocene relative sea-level changes inferred from multiple proxies on the west coast of South Korea. *Palaeoclimatol. Palaeoecol.* 496, 268–281. <https://doi.org/10.1016/j.palaeo.2018.01.044>.
- Spada, G., Melini, D., 2019. SELEN4 (SELEN version 4.0): a Fortran program for solving the gravitationally and topographically self-consistent sea-level equation in glacial isostatic adjustment modeling. *Geosci. Model Dev.* 12, 5055–5075. <https://doi.org/10.5194/gmd-12-5055-2019>.
- Sylvestre, F., Guiral, D., Debenay, J.P., 2004. Modern diatom distribution in mangrove swamps from the Kaw Estuary (French Guiana). *Mar. Geol.* 208, 281–293. <https://doi.org/10.1016/j.margeo.2004.04.012>.
- Tegmark, M., 1996. An Icosahedron-based method for pixelizing the celestial sphere. *Astrophys. J.* 470, L81–L84.
- Vink, A., Steffen, H., Reinhardt, L., Kaufmann, G., 2008. Holocene relative sea-level change, isostatic subsidence and the radial viscosity structure of the mantle of Northwest Europe (Belgium, the Netherlands, Germany, southern North Sea). *Quat. Sci. Rev.* 26, 3249–3275. <https://doi.org/10.1016/j.quascirev.2007.07.014>.
- Walker, M.J.C., Berkelhammer, M., Björck, S., Cwynar, L.C., Fisher, D.A., Long, A.J., Lowe, J.J., Newnham, R.M., Rasmussen, S.O., Weiss, H., 2012. Formal subdivision of the Holocene Series/Epoch: a Discussion Paper by a Working Group of INTIMATE (Integration of ice-core, marine and terrestrial records) and the Subcommittee on Quaternary Stratigraphy (International Commission on Stratigraphy). *J. Quat. Sci.* 27 (7), 649–659. <https://doi.org/10.1002/jqs.2565>.
- Wang, Z., Zhan, Q., Long, H., Saito, Y., Gao, X., Wu, X., Li, L., Zhao, Y., 2013. Early to mid-Holocene rapid sea-level rise and coastal response on the southern Yangtze delta plain, China. *J. Quat. Sci.* 28, 659–672. <https://doi.org/10.1002/jqs.2662>.
- Wang, F., Zong, Y., Mauz, B., Li, J., Fang, J., Tian, L., Chen, Y., Shang, Z., Jiang, X., Spada, G., Melini, D., 2020. Holocene Sea-level change on the central coast of Bohai Bay, China. *Earth Surf. Dyn.* 8, 679–693. <https://doi.org/10.5194/esurf-8-679-2020>.
- Watson, P.J., Lim, H.S., 2020. An update on the status of mean sea level rise around the Korean Peninsula. *Atmosphere*. 11, 1153. <https://doi.org/10.3390/atmos11111153>.
- Yokoyama, Y., Purcell, A., 2021. On the geophysical processes impacting palaeo-sea-level observations. *Geosci. Lett.* 8, 13. <https://doi.org/10.1186/s40562-021-00184-w>.
- Yoo, D.G., Lee, G.S., Kim, G.Y., Kang, N.K., Yi, B.Y., Kim, Y.J., Chun, J.H., Kong, G.S., 2016. Seismic stratigraphy and depositional history of late Quaternary deposits in a tide-dominated setting: an example from the eastern Yellow Sea. *Mar. Pet. Geol.* 73, 212–227. <https://doi.org/10.1016/j.marpetgeo.2016.03.005>.